THE JOURNAL OF PHYSICAL CHEMISTRY C

Article

pubs.acs.org/JPCC

Small-Angle Scattering Analysis of Empty or Loaded Hierarchical Porous Materials

Cedric J. Gommes,*[,†] Gonzalo Prieto,[‡,§] and Petra E. de Jongh[‡]

[†]Department of Chemical Engineering, University of Liège B6 A, 3 allée du 6 août, B-4000 Liège, Belgium

[‡]Inorganic Chemistry and Catalysis, Debye Institute for Nanomaterials Science, CG Utrecht University, NL-3584 Utrecht, The Netherlands

ABSTRACT: Small-angle scattering of X-rays (SAXS) or neutrons (SANS) is one of the few experimental methods that can in principle be used for the in situ study at the mesoscopic scale of physicochemical phenomena occurring inside nanoporous solids. However, the potential of the method is often limited by the lack of suitable data analysis methods to convert scattering data into real-space structural information. This is notably the case for most porous materials of practical interest, which exhibit a hierarchical structure with micro, meso, and macropores, with often a secondary material confined in the pores, such as in supported catalysts, as well as fuel-cell and battery materials. In the present paper, we propose a general analysis of X-ray scattering by this type of material. Assuming that each structural level is statistically independent from the others and has a distinct characteristic length scale, compact mathematical expressions are derived for the scattering of the entire hierarchical structure. The results are particularized to the SAXS analysis of SBA-15-ordered mesoporous silica loaded with copper nitrate as well as of supported catalysts obtained after heat treatment of that material. The SAXS data analysis shows that the nitrate fills both the micro- and mesopores of the material, while the metallic copper obtained after heat treatment is found only in the mesopores. Moreover, the mesoscopic-scale spatial distribution of the metal depends on the heat treatment, in line with earlier electron tomography studies. The main ideas underlying the SAXS data analysis were presented in a recent communication (Gommes et al. *Angew. Chem., Int. Ed.* **2015**, *54*, 11804−11808). Here, we generalize the approach and provide a comprehensive discussion of how any level in a hierarchical structure contributes to its overall scattering pattern. The results, as well as the general modeling methodology, will be of interest to anyone interested in the quantitative analysis of small-angle scattering data of empty or loaded porous solids and more generally of any type of hierarchical material.

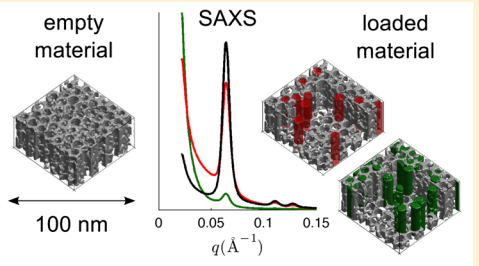

INTRODUCTION

A host of technologies and natural processes depend on physicochemical phenomena occurring inside nanometer-sized pores. A far from exhaustive list includes heterogeneous catalysis,[1,2] adsorptive separation processes,[3] energy storage technologies[4] including batteries, hydrogen storage,[5] and electrochemical processes,[6] the weathering of rocks,[7] and transport through biological membranes.[8] To improve the fundamental understanding of these phenomena as well as to drive further technological developments, experimental and analytical methods are needed to characterize these systems at the very scale at which the relevant phenomena take place.

Electron microscopy can provide a direct access to the morphology of nanostructures, sometimes in three dimensions.[9,10] However, the scope of microscopy is often limited by the electron dose that the samples can withstand. Moreover, the required high vacuum and the limited time-resolution of electron microscopy make it unsuitable to most in situ studies. Small-angle scattering (SAS) of X-rays (SAXS) or neutrons (SANS) is one of the few alternative experimental techniques that can be used to study nanostructures with nanometer resolution.[11,12] SAS is very flexible experimentally because the samples can be studied in a variety of chemical and physical environments[13−19] with a time resolution that can be as low as a few microseconds.[20] Moreover, compared to the femtogram of material that is characterized in a typical electron tomography study,[21] SAS provides a 12-decade enhancement of the sampling. The main difficulty with SAS, however, is the conversion of the scattering data into real-space structural information.

In a recent communication, we presented a SAXS analysis of copper catalysts supported on SBA-15 micro- and mesoporous silica.[21] That work required the modeling both of the empty porous material and of the mesopore-filling metal. The general assumptions of our approach consisted in assuming that any structural level in the material is statistically independent from the others and that it has a distinct characteristic length. In the present paper, we provide a comprehensive presentation of the methodology. In particular, we discuss thoroughly how the various structural levels in the hierarchical material contribute to the integrated intensity. We generalize the earlier models in order to allow some spatial correlation in the filling of the

Received: September 30, 2015
Revised: December 15, 2015
Published: December 29, 2015

DOI: 10.1021/acs.jpcc.5b09556
J. Phys. Chem. C 2016, 120, 1488−1506

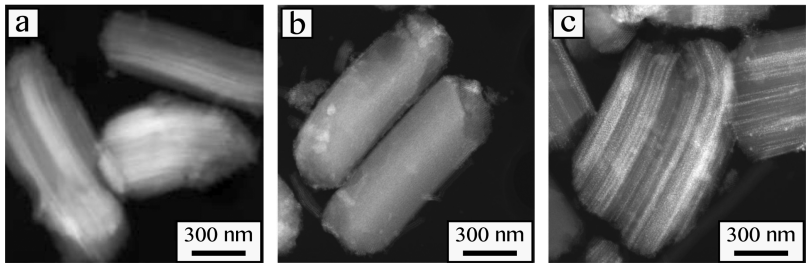

Figure 1. High-angle annular dark-field scanning-transmission electron microscopy (HAADF-STEM) images of Cu/Zn samples prepared similarly to Cu/S, Cu/S(N2), and Cu/S(NO), i.e., the nitrate-loaded SBA-15 (a) as well as samples heat-treated in N_2 (b) and in 2% NO (c). Micrograph in panel a was registered under cryogenic conditions (77 K) to prevent redistribution of the Cu nitrate filler under imaging conditions.

mesopores by the loading material. We also generalize the analysis to consider the case where the loading material can be present in both the meso- and the micropores.

The structure of the paper is as follows. In the first section, we present the materials that we use throughout the paper to illustrate the mathematical models, together with their experimental SAXS patterns. In the following section we present the general modeling methodology and underlying assumptions. We derive a general expression for the correlation function of a hierarchical micro/meso/macroporous material with a loading material contained in its pores. In the third section, we particularize the latter expression to the case of SBA-15 mesoporous silica. In that section, we consider first the case of empty SBA-15, and we develop a comprehensive model to analyze its SAXS in terms of both the micro and mesoporosity, as well as of its large-scale grain structure. Finally, that model is enhanced to account for the presence of loading material within the pores, and more specifically for its heterogeneity at the mesoscopic scale.

EXPERIMENTAL SECTION

The materials used to illustrate the SAXS data analysis methods developed in the present work are copper-loaded porous silicas. These materials were synthesized by impregnation of SBA-15-ordered mesoporous silica[22] with an aqueous solution of copper nitrate and subsequently dried, heat-treated, and reduced, according to a procedure thoroughly described elsewhere.[21] We refer hereafter to the dried, i.e., nitrate-loaded material as Cu/S. Starting from that material, two different metallic catalysts were prepared by decomposition of the Cu nitrate precursor via two different heat treatments. The material obtained with the heat treatment under N_2 flow is referred to as Cu/S(N2); the material obtained under 2% NO/N_2 flow is referred to as Cu/S(NO). Both materials were afterward reduced in hydrogen to produce supported Cu nanoparticles and thereby set the materials to their catalytically active state.

In all three materials, the overall metal loading is 0.18 g_{Cu}/g_{SiO2}. Nitrogen adsorption performed on the empty SBA-15 support (i.e., before impregnation) leads to a BET specific surface area of S_{BET} = 722 m^2/g and to a mesopore volume of V_{mes} = 0.70 cm^3/g. The pore size determined from adsorption is about 10 nm in diameter.

The type of heat treatment is known to have an effect on the spatial distribution of the metal in the final material.[23] For the purpose of illustration, Figure 1 shows dark-field transmission electron microscopy of materials prepared identically as described here for Cu/S, Cu/S(N_2), and Cu/S(NO) through additionally incorporating Zn as catalytic promoter of Cu.[24] On these images, the SBA-15 grains are visible with a typical width of 300 nm and length of about 1 μm. The mesopores are aligned with the long axis of the grains; they are not visible at the resolution of the figure. The pore-filling material, however, is sometimes visible as brighter zones inside the grains. In the nitrate-loaded material (Figure 1a), the elongated bright patches correspond to regions where the metal nitrate is present. For the sample heat-treated in the presence of NO some sharp features are also visible (Figure 1c), suggesting that the metal is present in specific mesopores while others are left empty. In the case of the sample heat-treated in pure N_2, the metal seems to be distributed uniformly throughout the grains, at a scale too small to be detected.

The small-angle X-ray scattering (SAXS) patterns of samples Cu/S, Cu/S(N_2), and Cu/S(NO) are shown in Figure 2. The

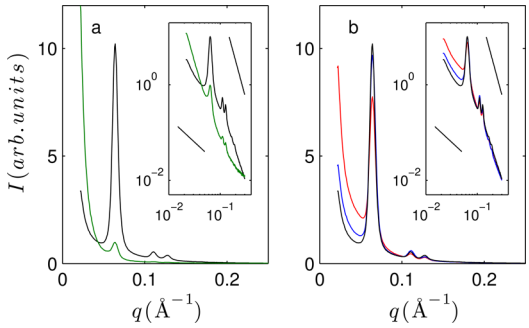

Figure 2. Small-angle scattering patterns measured on the empty SBA-15 (black), nitrate-loaded Cu/S (green), and heat-treated samples Cu/S (N2) (blue) and Cu/S(NO) (red). The data are plotted on double logarithmic scales in the insets, where the straight lines are power laws of the type $I \simeq q^{-4}$ (top) and $I \simeq q^{-1}$ (bottom).

samples were mounted in borosilicate glass capillaries, and the scattering patterns were measured on a XEUSS SAXS/WAXS setup from Xenocs, equipped with a molybdenum K-α source and a 2D detector. The 2D SAXS data were rotationally averaged using the ConeX software[25] and expressed as the scattered intensity as a function of the scattering wave vector $q = 4\pi/\lambda \sin(\theta/2)$, where θ is the scattering angle and λ = 0.71 Å is the wavelength. The SAXS patterns were corrected by subtracting the contribution of the empty capillary normalized by the transmitted intensity. Finally, because absolute intensities were not measured and to make the comparison easier between the various samples, the so-corrected SAXS patterns were normalized by the integrated intensity Q.[11]

The SAXS patterns in Figure 2 exhibit the scattering peaks typical of SBA-15,[26,27] the positions of which are characteristic of a structure with hexagonal P_{6mm} symmetry. The relative intensity of the peaks and of the background scattering,

DOI: 10.1021/acs.jpcc.5b09556
J. Phys. Chem. C 2016, 120, 1488−1506

however, is variable from one sample to another. In the case of the nitrate-loaded Cu/S sample, the peaks are very faint, and a $I \simeq q^{-4}$ diffuse scattering extends over the entire measured angular range. In the case of the metal-loaded samples Cu/S(NO) and Cu/S(N_2), the peaks remain sharper and the patterns differ mostly by the intensity of the $I \simeq q^{-1}$ background seen at low values of q. The latter background is more intense, by a factor as large as 2, in the case of the sample heat-treated in the presence of NO.

It has to be stressed that the low intensity of the peaks in Cu/S does not result from a damaging of the support during the impregnation because the peaks appear sharply again in Cu/S(N_2) and Cu/S(NO), which are obtained after heat-treatment and reduction of Cu/S. The faintness of the peaks possibly results from a contrast-matching effect between the silica and the nitrate, or from the presence of another type of nanostructure that would scatter strongly enough to cover the peaks. In the case of the metal-loaded samples, the difference in the $I \simeq q^{-1}$ background at low q is interesting. It hints at a more heterogeneous metal dispersion in Cu/S(NO) compared to Cu/S(N_2). This qualitative observation is in line with previous work[21] as well as with Figure 1.

CORRELATION FUNCTION OF LOADED MULTISCALE POROUS MATERIALS

When a nanostructured material is irradiated with X-rays, the intensity of the scattered beam depends on the spatial variation of the electron density $\rho(\mathbf{x})$, defined as the number of electrons per unit volume at point $\mathbf{x}$ in space.[11,12,28,29] Mathematically, the SAXS intensity $I(\mathbf{q})$ is equal to the Fourier transform of the electron-density correlation function, namely

$$I(\mathbf{q}) = \int e^{-i\mathbf{q}\cdot\mathbf{r}} \chi_\rho(\mathbf{r})\, dV_r \tag{1}$$

The correlation function χ_ρ is defined as the correlation between the electron density at any two points of the material at a distance $\mathbf{r}$ from one another, namely

$$\chi_\rho(\mathbf{r}) = \langle \rho(\mathbf{x}+\mathbf{r})\rho(\mathbf{x})\rangle - \langle\rho\rangle^2 \tag{2}$$

where the brackets stand for the average quantity, calculated over all possible values of $\mathbf{x}$. In the particular case of a loaded porous material, $\rho(\mathbf{x})$ takes the values 0, ρ_s, or ρ_l, according to whether point $\mathbf{x}$ is inside a pore, in the solid phase of the porous material, or in the loading. In eq 1, the bold-face characters indicate that the distances in reciprocal and real spaces are expressed with vectorial quantities $\mathbf{q}$ and $\mathbf{r}$, which is necessary for anisotropic structures such as SBA-15.

A direct consequence of eq 1 via Fourier's inversion theorem is that the integrated intensity Q, defined as the integral of $I(\mathbf{q})$ over the entire reciprocal space,[11,12] is related to the electron density correlation function via

$$Q = (2\pi)^3 \chi_\rho(0) \tag{3}$$

which is a relation that we shall use repeatedly in the present paper. The integrated intensity is also referred to as the *invariant* because it can be expressed simply in terms of the electron densities and volume fractions of the various phases present in the material, independently of the actual structure of the phases.[11] For a material comprising two phases A and B with electron densities ρ_A and ρ_B, and volume fractions ϕ_A and $\phi_B = 1 - \phi_A$, the relation is[11,12,29]

$$Q = (2\pi)^3 (\rho_A - \rho_B)^2 \phi_A \phi_B \tag{4}$$

and more general relations are available for more than two phases.[30] The case of neutron scattering is mathematically equivalent to X-ray scattering; only the electron density $\rho(\mathbf{x})$ is replaced by a nucleus-dependent scattering length density $b(\mathbf{x})$.[12]

In order to use a structure model to analyze small-angle scattering data, it is convenient to calculate first its correlation function $\chi_\rho(\mathbf{r})$. The type of nanostructure that we are interested in is shown in Figure 3. It consists of a solid that comprises

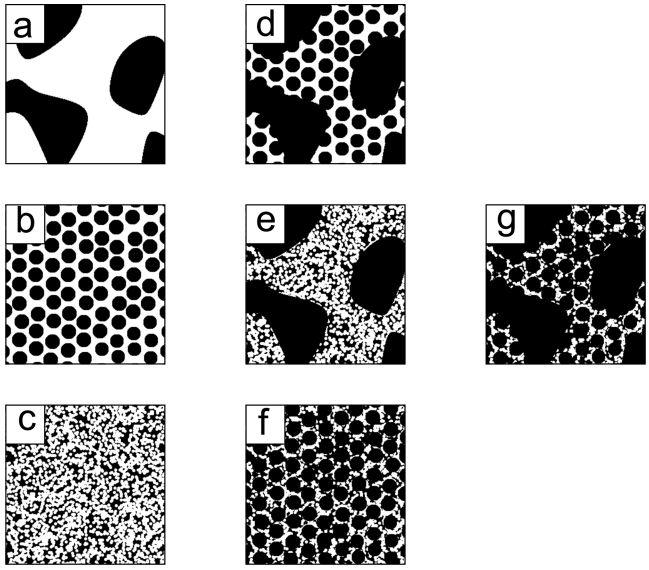

Figure 3. Various structural levels of the hierarchical model of porous material comprising (a) the macropores, (b) the mesopores, and (c) the micropores. The solid is shown in white and the pores in black. Each level is assumed to be statistically independent from the other two and to have a distinctive characteristic length. Combining selectively these structural levels, mathematical models are obtained for macro/meso (d), macro/micro (e), meso/micro (f), as well as for macro/meso/microporous materials (g).

micropores, mesopores, and macropores. We comply here with the recommendations of the International Union of Pure and Applied Chemistry.[31] Pores with sizes between 2 and 50 nm are referred to as mesopores. Smaller and larger pores are referred to as micropores and macropores, respectively. In addition to the structures shown in Figure 3, an additional level will be introduced later, corresponding to the pore-filling material.

The main challenge when developing a structural model is to keep it mathematically simple and yet realistic enough to analyze experimental data. This balance between mathematical simplicity and realism is best achieved through a probabilistic approach.[32,33] In a probabilistic context, defining a structural model consists in describing a set of statistical rules that can be used to generate a structure, rather than describing a specific structure itself. When applied to SAS data analysis, probabilistic models are suitable to describe not only the average features of the nanostructure but also the variability of the nanostructure over the entire volume of material that is sampled by the scattering experiment.

In the context of probabilistic models it is convenient to describe a given structure via its indicator function, which takes the value 1 when the point $\mathbf{x}$ is the phase and 0 otherwise.[32,34,35] For example, the first structural level that we

DOI: 10.1021/acs.jpcc.5b09556
J. Phys. Chem. C 2016, 120, 1488−1506

are concerned with is that of the micropores, the indicator function of which is defined as

$$\mu(\mathbf{x}) = \begin{cases} 1 & \text{if } \mathbf{x} \text{ is in a micropore} \\ 0 & \text{otherwise} \end{cases} \quad (5)$$

The indicator function $\mu(\mathbf{x})$ is defined mathematically as if the micropores were the only structure present in the material. This is illustrated in Figure 3c where the region with $\mu(\mathbf{x}) = 0$ (i.e., the solid) is shown in white and the micropores are shown in black. The micropores are notably characterized by their volume fraction ϕ_μ defined as

$$\phi_\mu = \langle \mu(\mathbf{x}) \rangle \quad (6)$$

and by their correlation function $\chi_\mu(\mathbf{r})$ defined as

$$\chi_\mu(\mathbf{r}) = \langle \mu(\mathbf{x}+\mathbf{r})\mu(\mathbf{x}) \rangle - \phi_\mu^2 \quad (7)$$

which is similar to eq 2. It is important to note that the micropore structure $\mu(\mathbf{x})$ is defined as if it filled the entire space. For example, in the case where other types of pores are present (e.g., Figure 3e–g) the actual fraction of space that is occupied by micropores is smaller than ϕ_μ.

The purpose of the present section is to calculate how the statistical characteristics of each structural level, ϕ and χ, combine to form the global correlation function $\chi_\rho(\mathbf{r})$, and this is independent of the specific probabilistic model used for each level. The second structural level is that of the mesopores with indicator function $m(\mathbf{x})$ (Figure 3b). The third structural level is that of the macropores, having indicator function $M(\mathbf{x})$ (Figure 3a). Using these notations, the indicator function of the solid phase in the micro/meso/macroporous material can be written as the product $[1 - \mu(\mathbf{x})][1 - m(\mathbf{x})][1 - M(\mathbf{x})]$, in which each factor accounts for a specific type of pore. This is illustrated in the third column of Figure 3. As mentioned previously, this model has to be complemented by the loading material, the indicator function of which we shall write $l(\mathbf{x})$. As far as X-ray scattering is concerned, the central property of each phase is its electron density ρ. The space-dependent electron density $\rho(\mathbf{x})$ can be written as follows in terms of the indicator functions

$$\rho(\mathbf{x}) = \rho_s[1 - M(\mathbf{x})][1 - \mu(\mathbf{x})][1 - m(\mathbf{x})] + \rho_l[1 - M(\mathbf{x})]l(\mathbf{x}) \quad (8)$$

where ρ_s and ρ_l are the electron densities of the solid and of the loading, respectively. Anticipating on the rest of the paper, the various contributions to $\rho(\mathbf{x})$ are illustrated in Figure 6 with the electron densities coded as colors. An implicit assumption in eq 8 is that the loading material is not present in the macropores but only in the micro- and mesopores. In the particular case of the samples of Figure 1, this is equivalent to assuming that there is no loading in the space between the SBA-15 grains. While this assumption is in all likelihood realistic for the examined system, it could be easily relaxed if necessary.

Using eq 8, the correlation function $\chi_\rho(\mathbf{r})$ can be expressed in terms of the auto- and cross-correlation functions of $\mu(\mathbf{x})$, $m(\mathbf{x})$, $M(\mathbf{x})$, and $l(\mathbf{x})$. In the following, we shall use the notation $P_{ab}(\mathbf{r})$ for the two-point probability function[30,36] of any two phases a and b, namely

$$P_{ab}(\mathbf{r}) = \langle a(\mathbf{x})b(\mathbf{x}+\mathbf{r}) \rangle \quad (9)$$

where $a(\mathbf{x})$ and $b(\mathbf{x})$ are the indicator functions of phases a and b. The function $P_{ab}(\mathbf{r})$ can be interpreted as the probability that two points at a distance $\mathbf{r}$ from one another belong one to phase a and the other to phase b. The same definition applies to the case $a = b$, in which case $P_{aa}(\mathbf{r})$ is the probability that the two points both belong to a. For very small distances $|\mathbf{r}|$ the two points necessarily belong to the same phase so that the probability is equal to the volume fraction of the phase, ϕ_a. For very large distances, one point belongs to a independently of the other, which leads to $P_{aa}(\mathbf{r} \to \infty) = \phi_a^2$. The correlation function $\chi_a(\mathbf{r})$ is related to $P_{aa}(\mathbf{r})$ via

$$\chi_a(\mathbf{r}) = P_{aa}(\mathbf{r}) - \phi_a^2 \quad (10)$$

It takes the value $\chi_a(0) = \phi_a(1 - \phi_a)$ and decreases toward the asymptotic value 0 over distances comparable to the characteristic length of the structure a.

The first simplifying assumption that we shall make is the statistical independence of the indicator functions $M(\mathbf{x})$, $m(\mathbf{x})$, and $\mu(\mathbf{x})$. For example, in the case of $M(\mathbf{x})$ and $m(\mathbf{x})$ this notably entails that the surface of a macropore can cut anywhere through a mesopore (see, e.g., Figure 3d). As a mathematical consequence, the averages of products can be factorized as in the following example

$$\langle M(\mathbf{x})m(\mathbf{x})M(\mathbf{x}+\mathbf{r})m(\mathbf{x}+\mathbf{r}) \rangle = P_{MM}(\mathbf{r})P_{mm}(\mathbf{r}) \quad (11)$$

which considerably simplifies the mathematics.

The second simplifying assumption is that each structural level has a distinctive characteristic length, which is very different from that of the others. The characteristic length can be given a precise meaning in the present context as the distance over which the corresponding correlation function $\chi(\mathbf{r})$ decreases to 0. For example, considering $\mu(\mathbf{x})$ and $m(\mathbf{x})$, a direct consequence of the assumption is that products of correlation functions can be approximated as follows

$$\chi_\mu(\mathbf{r})\chi_m(\mathbf{r}) \simeq \phi_m(1 - \phi_m)\chi_\mu(\mathbf{r}) \quad (12)$$

The reason for this is that $\chi_\mu(\mathbf{r})$ decreases to 0 over distances comparable with the characteristic length of $\mu(\mathbf{x})$, which is much shorter than that of $m(\mathbf{x})$. As a consequence, $\chi_m(\mathbf{r})$ can be considered as constant and equal to its value $\chi_m(0) = \phi_m(1 - \phi_m)$ in the product $\chi_\mu(\mathbf{r})\chi_m(\mathbf{r})$.

Using systematically the same type of simplification as in eqs 11 and 12, and assuming that the loading $l(\mathbf{x})$ is statistically independent of $M(\mathbf{x})$, eq 8 leads to the following expression for the electron-density autocorrelation function

$$\chi_\rho(\mathbf{r}) = [(1 - \phi_m)(1 - \phi_\mu)\rho_s + \rho_l\phi_l]^2\chi_M(\mathbf{r}) + \{\rho_s^2(1 - \phi_\mu)^2\chi_m(\mathbf{r}) + \rho_l^2\chi_l(\mathbf{r}) - 2\rho_s\rho_l\Gamma_{l\mu m}(\mathbf{r})\} (\chi_M(\mathbf{r}) + (1 - \phi_M)^2) + [(1 - \phi_m)(1 - \phi_M)] \rho_s^2\chi_\mu(\mathbf{r}) \quad (13)$$

where we have used the notation

$$\Gamma_{l\mu m}(\mathbf{r}) = \langle l(\mathbf{x}+\mathbf{r})\mu(\mathbf{x}) \rangle - \phi_l\phi_\mu + \langle l(\mathbf{x}+\mathbf{r})m(\mathbf{x}) \rangle - \phi_l\phi_m - \langle l(\mathbf{x}+\mathbf{r})\mu(\mathbf{x})m(\mathbf{x}) \rangle + \phi_l\phi_\mu\phi_m \quad (14)$$

The first and last terms in eq 13 account for the contributions of the macroporous and microporous structures to the overall electron-density correlation function, respectively. The second term is more complex as it involves the structures of the

DOI: 10.1021/acs.jpcc.5b09556
J. Phys. Chem. C 2016, 120, 1488–1506

mesopores, of the loading and of the macropores. We shall discuss the physical meaning of that term for specific types of loadings $l(\mathbf{x})$ in the following sections.

An important class of porous materials comes in the form of a powder with no macropore other than the spacing between the grains. This is notably the case for the catalysts of Figure 1. Moreover, the grains are generally larger than the lower resolution limit of the SAXS, so that the way in which the grains are positioned with respect to one another is irrelevant to the scattering data analysis. With no loss of generality, we may therefore assume that the grains are far from each other, in which case the correlation function of the large-scale structure can be approximated by

$$\chi_M(\mathbf{r}) \simeq \theta_g \Omega_g(\mathbf{r}) \tag{15}$$

where θ_g is the average number of grains per unit volume of the powder, and $\Omega_g(\mathbf{r})$ is the autocorrelation function of the individual grains.[34] The volume fraction of the large-scale structure is $\phi_M = 1 - \theta_g V_g$, where V_g is the average grain volume. Using these expressions and taking the limit of infinite dilution $\theta_g \to 0$, the electron correlation function takes the form

$$\frac{\chi_\rho(\mathbf{r})}{\theta_g} = [(1-\phi_m)(1-\phi_\mu)\rho_s + \rho_l\phi_l]^2\Omega_g(\mathbf{r}) + \{\rho_s^2(1-\phi_\mu)^2\chi_m(\mathbf{r}) + \rho_l^2\chi_l(\mathbf{r}) - 2\rho_s\rho_l\Gamma_{\mu m}(\mathbf{r})\} \Omega_g(\mathbf{r}) + V_g(1-\phi_m)\rho_s^2\chi_\mu(\mathbf{r}) \tag{16}$$

where the term proportional to $(1-\phi_M)^2$ in eq 13 no longer appears because it is of the second order in θ_g. The used approximations for ϕ_M and χ_M can be obtained rigorously as the low-density limit of Boolean models[34,37] (see also the Appendix).

The small-angle scattering intensity is obtained as the Fourier transform of eq 16 through eq 1. Each term in the expression of $\chi_\rho(\mathbf{r})$ has a clear structural significance. The first term in eq 16 accounts for the scattering by the grain as a whole, as if it had no substructure. The second term accounts for the scattering by the mesopores and the loading material. That contribution is the main subject of the present paper, but it cannot be discussed in general terms without specifying the model used to define $l(\mathbf{x})$. We therefore postpone its discussion to a following section. The entire second line is multiplied by $\Omega_g(\mathbf{r})$. This multiplication converts to a convolution in reciprocal space, which is eventually responsible for a size-broadening of the scattering peaks.[12,38] Finally, the last term, proportional to χ_μ accounts for the scattering by the micropores.

THE CASE OF EMPTY SBA-15 SILICA

The results obtained so far, and eq 16 in particular, are quite general and they apply to any type of porous material, provided the hierarchy of pores have distinctly different sizes and each structural level is statistically independent from the others. In order to show how they can be used practically to analyze SAXS data, we now particularize them to SBA-15 porous silica and use them for analyzing the data in Figure 2. We focus in the present section on the empty support, i.e., on the unloaded SBA-15 material.

Although SBA-15 is generally referred to as an ordered mesoporous material (OMM) with cylindrical pores,[39] its actual structure is much more complex. The mesopores are significantly corrugated[40] and the wall between them is microporous.[41] The typical value for the porosity of the wall is close to 35% and the overall mesoporosity is around 50%.[15,40,42] Numerous works have been concerned with the development of realistic models that account for the structural complexity of SBA-15, in the context of microscopy,[43] small-angle scattering,[44] and adsorption[45] studies, as well as for in situ scattering studies of adsorption phenomena.[46−48] We propose here a systematic approach that leads to analytical expressions that can be conveniently used to analyze scattering data.

As a first step in the SAXS analysis of structure as complex as SBA-15, it is useful to estimate the contribution of each structural level to the integrated intensity Q via eq 3 and eq 16. This leads to

$$\frac{Q}{(2\pi)^3\theta_g V_g} = [(1-\phi_\mu)(1-\phi_m)\rho_s]^2 + [(1-\phi_\mu)\rho_s]^2 \phi_m(1-\phi_m) + (1-\phi_m)\rho_s^2\phi_\mu(1-\phi_\mu) \tag{17}$$

where the three terms are the contributions of the large-scale structure, of the mesopores, and of the micropores, respectively. It is interesting to analyze the various terms in eq 17 in analogy with the general result for two phase systems eq 4. The first term is the squared electron-density contrast between the grains and the outside, calculated as if the grains were made up of a homogeneous phase. The absence of a term similar to $\phi_M(1-\phi_M)$ results from the normalization of the scattering per grain, corresponding to the term $\theta_g V_g$ in the denominator of the left-hand side of eq 17. The second term is exactly equivalent to eq 4 for the mesopore structure, with $\rho_A = 0$ in the mesopores and average electron density $\rho_B = (1-\phi_\mu)\rho_s$ outside the mesopores. Finally, the last term is a direct application of eq 4 to the microporous structure; it is multiplied here by $(1-\phi_m)$ because this is the fraction of space actually occupied by the microporous structure.

In order to compare the relative contribution of all structural levels to the overall scattered intensity of SBA-15, one can set $\rho_s = 1$ in eq 17 and focus on the effect of the volume fractions. Using the typical values $\phi_m \simeq 0.5$ and $\phi_\mu \simeq 0.35$, the values of the three terms are 0.106, 0.106, and 0.114. This shows that the grainlike large-scale structure, the mesoporous structure, and the microporous structure all contribute more or less equally to the SAXS of SBA-15. This is incidentally the reason for which structural models accounting exclusively for the mesoporous structure are unable to reproduce accurately the experimental scattering patterns of SBA-15.[49] In the coming three sections, we propose specific models for the three structural levels.

Large-Scale Structure. The large-scale structure of SBA-15 is that of the micrometer-sized grains. The corresponding scattering is calculated as the first term in eq 16. We shall write $I_g(\mathbf{q})$ as the Fourier transform of $\Omega_g(\mathbf{r})$. Because the grains are much larger than the lower resolution limit of small-angle scattering, it is sufficient to know only the asymptotic behavior of $I_g(\mathbf{q})$ for large values of q. The latter is given by Porod's formula, which has the form[11,50]

$$I_g(\mathbf{q}) \simeq \frac{2\pi A_g}{q^4} \tag{18}$$

where A_g is the outer surface area of the grain. When writing the latter expression we have implicitly assumed that the grain orientation is statistically isotropic, which is usually the case for

DOI: 10.1021/acs.jpcc.5b09556
J. Phys. Chem. C 2016, 120, 1488−1506

powders, so that it is the modulus $q = |\mathbf{q}|$ of the scattering wavevector that appears in the equation.

Micropores. The scattering from the micropores is calculated from the last term in eq 16. We write $I_\mu(\mathbf{q})$ as the Fourier transform of $\chi_\mu(\mathbf{r})$. Because the microporous structure of silica is disordered and isotropic, it is reasonable to model it via the following Guinier−Porod empirical model[51]

$$I_\mu(\mathbf{q}) = (2\pi)^3 \phi_\mu(1-\phi_\mu) R_\mu^3 f_{\mathrm{GP}}(qR_\mu) \tag{19}$$

where R_μ is a radius of gyration of the microporous silica, corresponding here to a characteristic size of the micropores, and $f_{GP}(x)$ is the following function

$$f_{\mathrm{GP}}(x) = \frac{1}{i_0} \times \begin{cases} e^{-x^2/3} & \text{for } x \le \sqrt{6} \\ e^{-2}36/x^4 & \text{for } x > \sqrt{6} \end{cases} \tag{20}$$

which satisfies Guinier's and Porod's laws for small and large values of q, respectively, and has a smooth transition between the two regimes. The value of the constant is $i_0 \simeq 46.36$, which guarantees that $\int_0^\infty 4\pi x^2 f(\mathbf{x})dx = 1$. The value of the prefactor in eq 19 was chosen in such a way that eq 4 is satisfied by $I_\mu(q)$.

For further purposes, it is useful to derive the relation between the parameters of the Guinier−Porod model and the specific surface area of the microporous structure. The latter is obtained in the usual way from the asymptotic expression of eq 19 via Porod's formula.[11,29] The following expression is obtained

$$S_\mu = \frac{e^{-2}36(2\pi)^2}{i_0} \frac{\phi_\mu(1-\phi_\mu)}{R_\mu} \tag{21}$$

The value S_μ is the specific surface area that would be observed if the microporous silica filled the entire space as in Figure 3c. The latter expression notably enables one to estimate the average chord length of the micropores as ϕ_μ/S_μ,[52] which is a better measure of micropore size than the radius of gyration R_μ.

Mesopores. The mesopores are the most salient features of SBA-15. They are approximately centered on the nodes of a 2D hexagonal lattice, which enables us to model their indicator function as

$$m(\mathbf{x}) = \sum_{n=1}^{\infty} f_n(\mathbf{x} - \mathbf{x}_n) \tag{22}$$

where the infinite sum is over all the nodes of the 2D lattice, $f_n()$ is a function that characterizes the size and shape of the nth mesopore, the position of which is $\mathbf{x}_n$. In order to account for the polydispersity of the pore sizes and for the elements of disorder in the lattice, we consider $f_n()$ and $\mathbf{x}_n$ as random functions, which we shall explicit shortly. Moreover, we shall use the customary assumption that two distinct pores are statistically independent of one another.[27,38,43]

With this particular form for $m(\mathbf{x})$, the correlation function of the mesopores $\chi_m(\mathbf{x})$ can be written as

$$\chi_m(\mathbf{r}) = \sum_n \sum_m \langle f_n(\mathbf{x} - \mathbf{x}_n) f_m(\mathbf{x} - \mathbf{x}_m + \mathbf{r}) \rangle - \phi_m^2 \tag{23}$$

Estimating the Fourier transform of eq 23 leads to the classical expression[27,38,53]

$$I_m(\mathbf{q}) = \theta_m \{ |\langle F(\mathbf{q}) \rangle|^2 (Z'(\mathbf{q}) - 1) + \langle |F(\mathbf{q})|^2 \rangle \} \tag{24}$$

where θ_m is the average number of mesopores per unit area of the plane orthogonal to them, $F(\mathbf{q})$ is the Fourier transform of $f(\mathbf{x})$, and the brackets $\langle\rangle$ have to be understood as the average over all the mesopores or equivalently as the ensemble average over all possible realizations of any given mesopore. The lattice factor $Z'(\mathbf{q})$ is defined here as

$$Z'(\mathbf{q}) = \lim_{N\to\infty} \frac{1}{N} \sum_{n=1}^{N} \sum_{m=1}^{N} e^{-i\mathbf{q}\cdot(\mathbf{x}_n - \mathbf{x}_m)} - (2\pi)^2 \theta_m \delta(\mathbf{q}) \tag{25}$$

which describes the relative position of the mesopores with respect to one another. The second term in eq 25 is usually absent in the definition of the lattice factor. Its presence here is a consequence of the subtraction of ϕ_m^2 in eq 23, which results in the removal of the singularity that would otherwise be present in the lattice factor for $q \to 0$. Our convention in the present paper is to write $Z'(\mathbf{q})$ as the lattice factor with the singularity removed as in eq 25 and $Z(\mathbf{q})$ when the singularity is present (see Figure 11 in the Appendix). Moreover, we refer to the term proportional to $Z'(\mathbf{q})$ in eq 24 as the coherent contribution and to the remainder, i.e., $\langle |F(\mathbf{q})|^2 \rangle - |\langle F(\mathbf{q}) \rangle|^2$, as the incoherent contribution. The latter contribution would vanish in the case where all the mesopores would be identical.

Equation 24 was calculated as if the grain was infinite, i.e., neglecting the factor $\Omega_g(\mathbf{r})$ in eq 16. As mentioned previously, the result still has to be convoluted with the Fourier transform of $\Omega_g(\mathbf{r})$, i.e., with $I_g(\mathbf{q})$. We have to consider separately the effect of the convolution on the coherent and incoherent contributions to $I_m(\mathbf{q})$. Because the grain is much larger than the mesopores, the convolution does not deform the incoherent scattering significantly; the only significant effect is a multiplication by the volume of the grain $V_g = \Omega_g(0)$. Therefore, the incoherent scattering per grain is obtained by replacing θ_m by the number of mesopores in a grain, namely $N = \theta_m V_g$. The same multiplicative correction applies to the coherent scattering as well. In addition, the convolution of the otherwise infinitely thin scattering peaks in $Z'(\mathbf{q})$ leads to a size-broadening. Suitable approximations for the lattice factor of 2D hexagonal lattices, with size broadening effects, are given in the Appendix. It has to be stressed that in the case where the lattice factor $Z(\mathbf{q})$ would be wrongly used in place of $Z'(\mathbf{q})$, the convolution of the singularity at the origin with the Fourier transform of $\Omega_g(\mathbf{r})$ would lead to a term that is redundant with the scattering of by the large-scale structure $I_g(\mathbf{q})$.

The other factor that enters the expression for the scattering by the mesopores eq 24, besides the structure factor, is their form factor $F(\mathbf{q})$. Assuming cylindrical mesopores with radius R and height H, the Fourier transform of $f(\mathbf{x})$ is given by the classical expression[27,54]

$$F(\mathbf{q}) = \pi R^2 H \frac{2J_1(|\mathbf{q}_\perp| R|)}{|\mathbf{q}_\perp| R|} \frac{\sin(\mathbf{q}_z H/2)}{\mathbf{q}_z H/2} \tag{26}$$

where $J_1()$ is the first-order Bessel function of the first kind, and we have used the notations $\mathbf{q}_z$ and $\mathbf{q}_\perp$ for the components of the scattering vector parallel and perpendicular to the mesopore.

Unlike eqs 18 and 19, the expression for the scattering by the mesopores is anisotropic. Before eq 24 can be used to analyze powder scattering patterns, it has therefore to be averaged over all possible orientations of the grain. The classical procedure would consist in using a sine-integral function in the form factor of the mesopores.[11] In the particular case of SBA-15, however, we show in the Appendix that the averaging procedure can be done in a much simpler way by setting $\mathbf{q}_z$

DOI: 10.1021/acs.jpcc.5b09556
J. Phys. Chem. C 2016, 120, 1488−1506

= 0, replacing $\mathbf{q}_\perp$ by the modulus $q = |\mathbf{q}|$ and multiplying the result by $\pi/(qH)$.

SAXS Analysis of Empty SBA-15 Silica. If one gathers the particular expressions for the scattering by the large-scale structure, by the micropores and by the mesopores into eq 16, the following expression is eventually obtained for the SAXS intensity of the empty SBA-15

$$I(\mathbf{q}) = [(1-\phi_m)(1-\phi_\mu)\rho_s]^2 \frac{2\pi A_g}{q^4} + N[\rho_s(1-\phi_\mu)]^2 \frac{\pi H}{q}\left\{\left|\left\langle \pi R^2 \frac{2J_1(qR)}{qR}\right\rangle\right|^2 [Z'(q)-1] + \left\langle \left|\pi R^2 \frac{2J_1(qR)}{qR}\right|^2 \right\rangle\right\} + V_g(2\pi)^3\rho_s^2(1-\phi_m)\phi_\mu(1-\phi_\mu) R_\mu^3 f_{GP}(qR_\mu) \quad (27)$$

This expression is comprehensive: it accounts for the large-scale grain structure of the material, for the mesopore structure, as well as for the microporosity of the pore walls. The complete model is adjustable through many parameters, which can in principle all be used to fit the SAXS data of empty SBA-15. Allowing all the parameters to be adjusted, however, would result in an unreliable fit due to the too many degrees of freedom. Fortunately, the structure of SBA-15 is known well enough from earlier works for many parameters to be either fixed or at least for bounds to be set on their values. We now consider successively all the parameters that describe the structure, going from the larger to the smaller scales.

The largest structure is that of the grains. Their size and shape is specified through their height H and diameter D. Because both are much larger than the lower resolution of the SAXS, we assumed the values D = 500 nm and H = 1000 nm, based on the micrographs of Figure 1 and also on previous studies.[55] The volume and outer surface area of the grains are calculated assuming they are cylinders, $V_g = \pi D^2 H/4$ and $A_g = \pi D^2/2 + \pi DH$.

The parameters that describe the mesopore structure are of two types. On one hand, the parameters describing the mesopores individually are their average radius R_m and the standard deviation σ_R, assuming a Gaussian size distribution. On the other hand, the parameters describing the positioning of the mesopores are the spacing a of the lattice, a Debye−Waller parameter σ_a accounting for the statistical deviation of the mesopores from the ideal lattice,[56] as well as two parameters δ and ν describing the width and shape of the peaks in the lattice factor (see the Appendix). The spacing a is unambiguously determined from the position of the peaks in the scattering pattern. The radius R_m is left as an adjustable parameter, but we know from nitrogen physisorption that it should be close to 50 Å. As far as scattering is concerned, the two parameters σ_R and σ_a have similar effects: they both contribute to reduce the intensity of the higher-order scattering peaks.[26,40] Because it would be impossible to discriminate the effects of σ_R and of σ_a from a fit, we decided to fix σ_a = 0 and keep σ_R as an adjustable parameter. Moreover, it is known from previous work that the order of magnitude of σ_R is 5 Å.[25,40,44] This value corresponds approximately to half the thickness of the so-called corona, which is an early model used to account for this type of disorder.[26,57] The number of mesopores N and the mesopore volume fraction ϕ_m that appear in eq 27 do not require additional degrees of freedom for the fit. They are calculated as $N = (\pi D^2/4)/(\sqrt{3}a^2/2)$ and $\phi_m = \pi(R_m^2 + \sigma_R^2)/(\sqrt{3}a^2/2)$ where the denominator in both expressions is the area of a cell of the 2D hexagonal lattice.

Concerning the microporous structure, it is completely characterized by the two parameters ϕ_μ and R_μ. The value of ϕ_μ is known from a variety of characterization techniques—nitrogen adsorption,[40] electron tomography,[43] mechanical properties[42]—to be close to ϕ_μ = 0.35. We fixed this parameter to that particular value. The single adjustable parameter is therefore R_μ, which we know should be close to 20 Å because it is related to the size of the micropores.[31]

The least-squares fit of the SAXS data of empty SBA-15 is presented in Figure 4. The main parameters of the model take

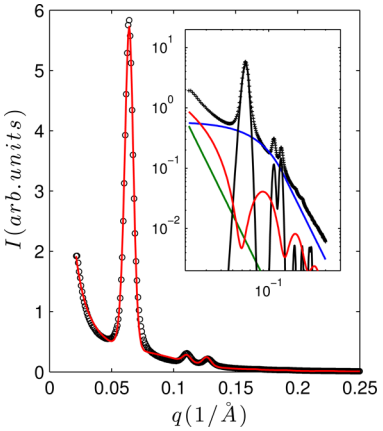

Figure 4. SAXS pattern of the empty SB-15 (dots) and best fit with eq 27 (red). The inset shows on logarithmic scales the contributions of coherent scattering (black), incoherent scattering (red), microporous structure (blue), and Porod scattering of the grain (green).

the following values: a = 110 Å, R_m = 43 Å, σ_R = 5.0 Å, and R_μ = 23 Å. Interestingly, the width of the peaks δ is about two times larger than what would be obtained from the Debye−Scherrer relation from the diameter of the grain D. This points to a significant distortion of the lattice, in addition to the size-broadening.

In order to check the realism of the fitted parameters, it is interesting to use them to calculate a few structural characteristics of the material. The radius of gyration of the microporous structure R_μ converts to an average micropore chord length $\phi_\mu/S_\mu \simeq 0.9$ nm. Concerning the mesopore volume, it is calculated as[43]

$$V_m = \frac{\pi(R_m^2 + \sigma_R^2)}{[a^2\sqrt{3}/2 - \pi(R_m^2 + \sigma_R^2)](1-\phi_\mu)\tilde{\rho}_{SiO2}} \quad (28)$$

where $\tilde{\rho}_{SiO2}$ is the specitic mass of silica. Using the value $\tilde{\rho}_{SiO2}$ = 2.2 g cm^{-3}, the value derived from the SAXS is V_m = 0.7 cm^3/g, which is in perfect agreement with the value V_m = 0.7 cm^3/g obtained from nitrogen adsorption (see the Experimental Section). As for the specific surface area, it is calculated as follows:

$$S = \frac{[a^2\sqrt{3}/2 - \pi(R_m^2 + \sigma_R^2)]S_\mu + 2\pi R_m(1-\phi_\mu)}{[a^2\sqrt{3}/2 - \pi(R_m^2 + \sigma_R^2)](1-\phi_\mu)\tilde{\rho}_{SiO2}} \quad (29)$$

The first term in the numerator is the contribution of the microporous structure, and the second term is the contribution

DOI: 10.1021/acs.jpcc.5b09556
J. Phys. Chem. C 2016, 120, 1488−1506

of the mesopores. The value inferred from the SAXS is 588 m^2/g, which falls slightly short of the 720 m^2/g obtained from nitrogen adsorption. The difference stems from the inability of eq 19 to describe the scattering at very large q (see the blue curve in the inset of Figure 4). If necessary, this could be improved by using a more complex function than eq 19 to describe the microporous structure.

A realization of the model of SBA-15 with all parameters determined from the fit of the SAXS data is shown in Figure 5.

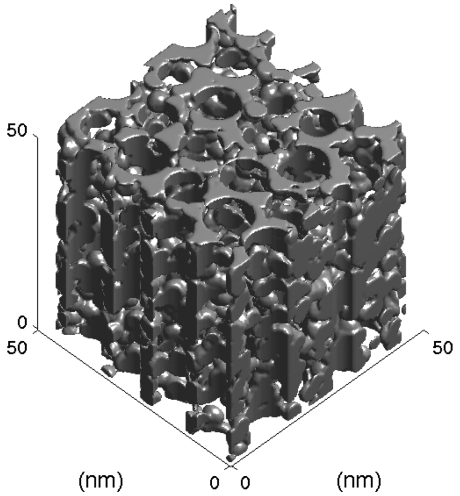

Figure 5. Realization of our model of SBA-15, with all parameters determined from the fit of the SAXS data of Figure 4.

The empirical Guinier–Porod function used to model $I_\mu(q)$ does not correspond to any existing structure. For the purpose of illustration, the microporous silica shown in Figure 5 was obtained as a Boolean process[34] having the same density and surface area as in eq 19. In addition to being in quantitative agreement with both SAXS data and nitrogen adsorption, the visual similarity of the model with electron tomography reconstructions of SBA-15 is striking.[24,40,58]

THE CASE OF COPPER-LOADED SBA-15

We proceed here to extend the model of empty SBA-15 in order to analyze the SAXS of the loaded samples Cu/S, Cu/S(NO), and Cu/S(N_2) of Figure 2. The general expression that we have derived for the correlation function of the electron density eq 16 remains valid but we have to make it more specific by defining explicitly the statistical rules for generating the indicator function $l(\mathbf{x})$ of the loading material. This will enable us to have analytical forms for the correlation function $\chi_l(\mathbf{r})$ and for the cross-correlation function $\Gamma_{l\mu m}(\mathbf{r})$, which is necessary to fit the SAXS data.

The material that fills the pores of the porous silica discussed in Figure 1 is itself possibly structured at the nanometer scale. This clearly applies to metallic copper which comes in the form of nanoparticles, and this may also be the case for the nitrate, which might be present in the form of crystallites, as layers covering the pore walls, etc. However, the main purpose of the present work is to describe the mesoscale heterogeneity of the loading. For example, we are interested in determining whether a given type of pore is loaded at all, while the actual structure of the loading within the pore is irrelevant. In the following, we shall therefore treat the loading material as if it were a homogeneous phase with average electron density ρ_l.

The average electron density of the equivalent homogeneous pore-filling phase ρ_l cannot take arbitrary values. On one hand, it cannot exceed the electron density of the actual pore-filling material, whose quantity we refer to as $\rho_l^{\max}$. On the other hand, ρ_l cannot be arbitrarily low either. The lowest possible value corresponds to the case where the known macroscopic loading of the material would be homogeneously spread over the entire available pore volume. The average density ρ_l of the loading phase and its volume fraction ϕ_l are related to each other via the following inverse relation

$$\rho_l = \rho_l^{\max} \frac{\phi_l^{\min}}{\phi_l} \tag{30}$$

where $\phi_l^{\min}$ is the volume fraction of the loading that would correspond to $\rho_l^{\max}$. If ρ_l and ϕ_l are modified in such a way that eq 30 is satisfied, then the macroscopic loading of the material is left unchanged.

The values of $\rho_l^{\max}$ and $\phi_l^{\min}$ relevant to Cu/S, Cu/S(NO), and Cu/S(N_2) are gathered in Table 1. The estimates are based on the macroscopic loading of $0.18 g_{Cu}/g_{SiO2}$. The electron densities of the various materials are calculated in the usual way from the mass density $\tilde{\rho}$, the molar mass M, and the number of electrons Ne^- in one mole of material.[59] The electron density of the silica that forms the support is ρ_{SiO2} = 1.1 $F{\cdot}cm^{-3}$ (Faraday per cubic centimeter). In the case of Cu/S, several crystallographic forms are possible for the nitrate, with different electron densities. We assumed the anhydrous form with formula Cu $(NO_3)_2$. In the case of the reduced samples, only metallic copper is considered, with a known electron density.

Loading Model 1: Mesopore Filling. The first model that we shall consider to analyze the SAXS data of Figure 2 consists in loading randomly each mesopore with a prescribed probability, and leaving the micropores empty. This is illustrated in Figure 6b,c. The corresponding indicator function can be written formally as

$$l(\mathbf{x}) = \sum_{n=1}^{\infty} \Lambda_n f_n(\mathbf{x} - \mathbf{x}_n) \tag{31}$$

where $f_n(\mathbf{x})$ has the same meaning as in eq 22 and Λ_n is a random variable that determines whether the nth mesopore is loaded or not. For example, the particular model where any

Table 1. Characteristics of the Materials Relevant to the SAXS Data Analysis[a]

	formula	Ne^-	M ($g\ mol^{-1}$)	$\tilde{\rho}$ ($g{\cdot}cm^{-3}$)	$\rho_l^{\max}$ ($F{\cdot}cm^{-3}$)	$\phi_l^{\min}$ (−)
silica	SiO_2	30	60.0	2.2	1.10	[b]
copper	Cu	29	63.5	9.0	4.09	0.012
copper nitrate	$Cu(NO_3)_2$	91	187.5	3.05	1.48	0.13

[a]The last two columns are the values used to calculate the average electron density of the loading ρ_l through eq 30. Key: Ne^-, number of electrons; M, molar mass; $\tilde{\rho}$, specific mass; $\rho_l^{\max}$ electron density of the dense material; $\phi_l^{\min}$, volume fraction of the dense material assuming an overall loading of 0.18 g_{Cu}/g_{SiO2}. [b]Nonapplicable.

DOI: 10.1021/acs.jpcc.5b09556
J. Phys. Chem. C 2016, 120, 1488−1506

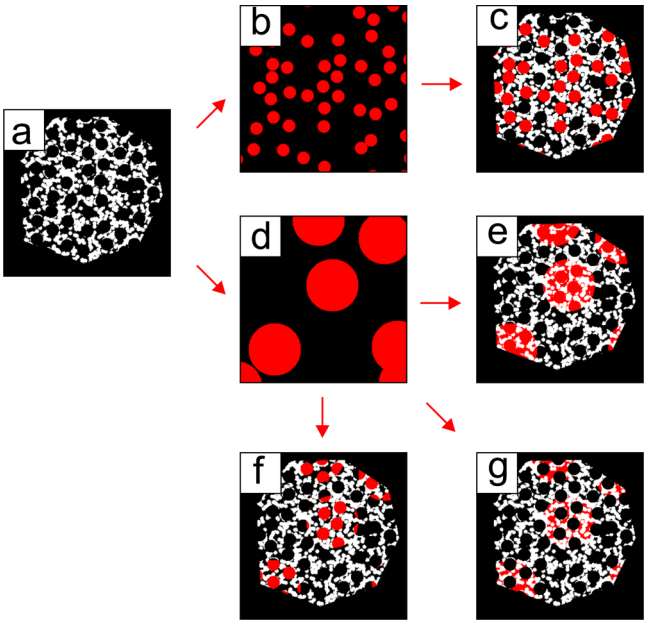

Figure 6. Starting from a given empty SBA-15 model (a), two loading models are considered. In the mesopore-filling model (b, c), the mesopores are chosen randomly and filled. In the loading-patch model (d), the loading comes in the form of patches and it fills locally all the pores (e), only the mesopores (f), or only the micropores (g). The complete electron density is obtained by combining the loading and the support; the different colors symbolize here different electron densities.

individual mesopore would be loaded or left empty according to a head-or-tail rule corresponds to the case where the Λ_n's are independent random variables taking the values 0 and 1 with probability 1/2.

In the frame of the present mesopore-filling model, the volume fraction of the loading phase is calculated as

$$\phi_l = \langle\Lambda\rangle\phi_m \tag{32}$$

where ϕ_m is the volume fraction of the mesopores. This results from the observation that $\langle\Lambda\rangle$ is equal to the probability for any pore to be loaded. SAXS is also sensitive to the correlation between the loading of various mesopores, which is characterized by the quantity $\langle\Lambda_n\Lambda_m\rangle$. If the loading of any two given pores were uncorrelated, the loading variables would satisfy $\langle\Lambda_n\Lambda_m\rangle = \langle\Lambda\rangle^2$ for $n \neq m$ and $\langle\Lambda_n\Lambda_n\rangle = \langle\Lambda^2\rangle$. In order to allow for the possibility of correlated loading, we write

$$\langle\Lambda_n\Lambda_m\rangle = \langle\Lambda\rangle(1 - \langle\Lambda\rangle)g_{mn} + \langle\Lambda\rangle^2 \tag{33}$$

which can be considered as the definition of the correlation function g_{mn}. For the purpose of fitting the SAXS data, it is reasonable to assume an exponential correlation of the type

$$g_{mn} = \exp(-d_{mn}/l_C) \tag{34}$$

where d_{mn} is the distance between pores m and n and l_C is a correlation length. The case of uncorrelated random loading is obtained for vanishingly small correlation lengths, for which one recovers $g_{mn} = \delta_{mn}$ where δ_{mn} is Kronecker's symbol. This is the model assumed in our earlier work on Cu/SiO_2 catalysts[21] as well as by Erko et al. in the context of in situ small-angle neutron scattering study of capillary condensation.[60] We consider here a more general case: finite values of l_C correspond to a statistical segregation of loaded and unloaded mesopores over distances comparable with l_C. Correlation effects can also be understood as the apparent clustering of loaded mesopores.

With a loading of the type of eq 31, the indicator function $l(\mathbf{x})$ is independent of the indicator function of the micropores $\mu(\mathbf{x})$, which enables us to rewrite the cross-correlation function eq 14 as

$$\Gamma_{l\mu m}(\mathbf{r}) = (1 - \phi_\mu)(P_{lm}(\mathbf{r}) - \phi_l\phi_m) \tag{35}$$

Introducing this relation in eq 13, and using the same type of calculations as with the empty SBA-15 model, the following expression is eventually obtained for the SAXS intensity

$$\begin{aligned} I(\mathbf{q}) = {} & [(1 - \phi_m)(1 - \phi_\mu)\rho_s + \rho_l\phi_l]^2\frac{2\pi A_g}{q^4} \\ & + N[\rho_l\langle\Lambda\rangle - \rho_s(1 - \phi_\mu)]^2\{|\langle F(\mathbf{q})\rangle|^2 \\ & [Z'(\mathbf{q}) - 1] + \langle|F(\mathbf{q})|^2\rangle\} + V_g(1 - \phi_m)\rho_s^2 I_\mu(q) \\ & + N\rho_l^2\langle\Lambda\rangle(1 - \langle\Lambda\rangle)\{|\langle F(\mathbf{q})\rangle|^2[Z_g(\mathbf{q}) - 1] \\ & + \langle|F(\mathbf{q})|^2\rangle\} \end{aligned} \tag{36}$$

In this expression, $Z_g(\mathbf{q})$ is a structure factor limited to the loaded mesopores. It is defined as

$$Z_g(\mathbf{q}) = \lim_{N\to\infty}\frac{1}{N}\sum_{n=1}^{N}\sum_{m=1}^{N} g_{mn}e^{-i\mathbf{q}\cdot(\mathbf{x}_n - \mathbf{x}_m)} \tag{37}$$

which reduces to $Z_g(q) = 1$ in the case of uncorrelated mesopore-filling. In the more general case of an exponential correlation with correlation length l_C, the expression is given in eq 53 of the Appendix. Following the same notation as in eq 25, we refer to that expression as $Z_g(\mathbf{q},l_C)$ or $Z'_g(\mathbf{q},l_C)$ according to whether the central scattering at the origin is present or not. Note that in eq 36 the central scattering is present in the last term but not in the second. In the case of correlated mesopore filling the central scattering in $Z_g(\mathbf{q})$ accounts for the scattering by clusters of loaded mesopores.

It is interesting to split the various contributions in eq 36 into two groups. On one hand, the first three terms are already present in the SAXS of the empty material (see eq 27). They appear here with different prefactors because the apparent electron-density contrasts relevant to the various structural levels are modified by the sheer presence of a loading material in the pores. On the other hand, the last term is new: it accounts for the additional scattering by the loading material itself. We refer to the modified prefactors as contrast matching corrections. In order to understand the relative importance of these effects on the overall scattered intensity it is useful to estimate the integrated intensity Q, which can be done from eqs 3 and 16. The specificity of the mesopore-filling model comes from eq 35, from which we obtain $\Gamma_{l\mu m}(0) = (1 - \phi_\mu)(1 - \phi_m)\phi_l$. Gathering the terms in the same order as in eq 36, the following expression is obtained

$$\begin{aligned} \frac{Q}{\theta_g V_g(2\pi)^3} = {} & [(1 - \phi_m)(1 - \phi_\mu)\rho_s + \phi_l\rho_l]^2 \\ & + [\rho_l\langle\Lambda\rangle - \rho_s(1 - \phi_\mu)]^2\phi_m(1 - \phi_m) + (1 - \phi_m)\rho_s^2 \\ & \phi_\mu(1 - \phi_\mu) + \phi_m\rho_l^2\langle\Lambda\rangle(1 - \langle\Lambda\rangle) \end{aligned} \tag{38}$$

This expression can be analyzed in the same way as eq 17 by analogy with eq 4 that is valid for two-phase systems. The first

DOI: 10.1021/acs.jpcc.5b09556
J. Phys. Chem. C 2016, 120, 1488−1506

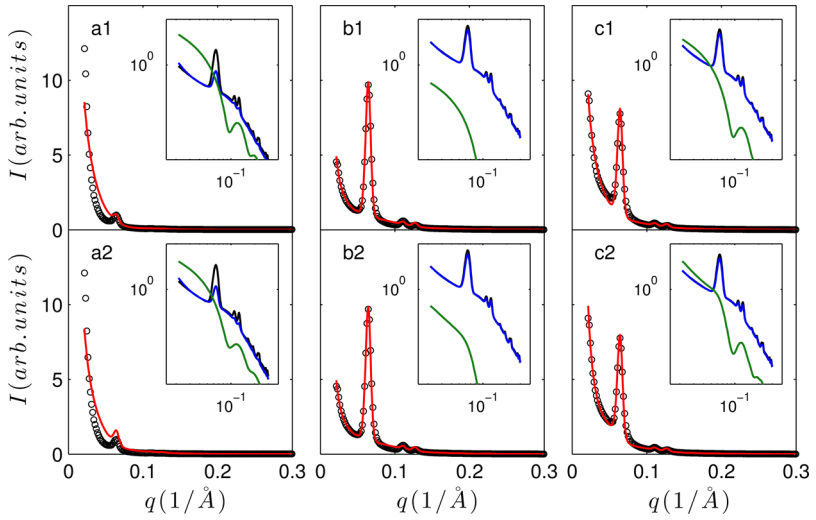

Figure 7. Fitting of the SAXS data of nitrate-loaded Cu/S (a1−a2) as well as of metal-loaded Cu/S(N2) (b1−b2) and Cu/S(NO) (c1−c2) with the mesopore-filling model (model 1) corresponding to eq 36. The symbols are the data, and the solid red line is the least-squares fit with the uncorrelated loading (l_C = 0 top row) and correlated loading (finite l_C, bottom row). The components of the best fit are shown in the insets on double-logarithmic scales: scattering by the loaded mesopores (green) and by the porous support with contrast-matching corrections (blue). For comparison, the SAXS of the empty support is shown in black. In the case of the metal-loaded samples, the blue and black curves are indistinguishable at the scale of the figure, pointing at insignificant contrast-matching effects.

term is the squared average electron density of the grain: it accounts for the scattering by the grain structure. The second term is a product of two factors. The first is the squared average electron density contrast between the inside of the partially loaded mesopores, with $\rho_A = \langle\Lambda\rangle\rho_l$, and the surrounding microporous silica, with $\rho_B = (1 - \phi_\mu)\rho_s$. The second factor is the usual product $\phi_m(1 - \phi_m)$. The third term is the scattering by the loading itself. The volume fraction is replaced here by the loading probability $\langle\Lambda\rangle$, and the term is multiplied by ϕ_m which is the fraction of space that is relevant to loading. The last term is unchanged compared to eq 17 because the loading material is not allowed in the micropores in the context of the present mesopore-filling model.

The simplest version of the present model consists in assuming uncorrelated mesopores filling, corresponding to $g(d) = 0$. The SAXS patterns of the metal-loaded samples Cu/S(N_2) and Cu/S(NO) can be satisfactorily fitted with that simple model (Figure 7b1 and c1). The fit of the data was done by setting $Z_g(\mathbf{q}) = 1$ in eq 36 and keeping all the parameters of the support equal to the values obtained from the fit of the empty SBA-15 data (see Figures 4 and 5). The only fitting parameter was therefore the loading probability $\langle\Lambda\rangle$ or equivalently $\phi_l = \langle\Lambda\rangle\,\phi_m$, with $\phi_m \simeq 0.48$ for the SBA-15 material used here. For any value of ϕ_l, the electron density ρ_l was calculated through eq 30. The values of ϕ_l obtained from the fit are reported in Table 2: the corresponding loading probabilities are $\langle\Lambda\rangle = 0.11$ for Cu/S(NO) and $\langle\Lambda\rangle = 0.73$ for Cu/S(N_2). These values mean that the copper uniformly spreads over about 73% of the mesopores in the case of N_2 heat treatment, while in the presence of NO it concentrates into about 11% of them. This significant difference in the metal dispersion is in qualitative agreement with both Figure 1 and with the 3DTEM characterization of these samples.[21]

Interestingly, the SAXS of the nitrate-loaded sample Cu/S cannot be fitted satisfactorily with the uncorrelated pore model (Figure 7a1). The model remains inaccurate even when finite correlation effects are allowed through eq 34, i.e., when the correlation length l_C is used as an adjustable parameter in the fit

Table 2. Values of the Structural Parameters of the Various Loading Models, Obtained from the Least-Square Fits of the SAXS Data of Samples Cu/S, Cu/S(N2), and Cu/S(NO)

		Cu/S	Cu/S(N_2)	Cu/S(NO)
mesopore filling:				
uncorrelated	error[a] (%)	129	8	20
(l_C = 0)	ϕ_l	0.13	0.35	0.05
correlated	error[a] (%)	175	9	9
(finite l_C)	ϕ_l	0.13	0.31	0.03
	l_C (nm)	6	4	5
loading patches:				
all-pore loading	error[a] (%)	32	21	36
(ϵ_1 = 1, ϵ_2 = 1)	ϕ_l	0.13	0.1	0.014
	l_C (nm)	5	23	22
mesopore loading	error[a] (%)	93	11	20
(ϵ_1 = 1, ϵ_2 = 0)	ϕ_l	0.13	0.21	0.03
	l_C (nm)	5	22	11
micropore loading	error[a] (%)	302	16	28
(ϵ_1 = 0, ϵ_2 = 1)	ϕ_l	0.13	0.012	0.012
	l_C (nm)	5	27	6

[a]The error is the largest relative difference between the fitted spectrum and the data for $q \leq 0.06$ Å^{-1}.

(Figure 7a2). The main difference between the data and the model is the different overall power-law exponent of the scattering, as visible from the inset of Figure 7a1 and a2. The mesopore-loading model leads to a background scattering of the type $I \sim q^{-1}$, while the experimental SAXS of the nitrate-loads sample Cu/S is characterized by an overall Porod-like q^{-4} scattering (see inset of Figure 2a).

In the case of the metal-loaded materials Cu/S(N_2) and Cu/S(NO), using the correlation length l_C as an adjustable parameter in addition to $\langle\Lambda\rangle$ leads to a slight improvement of the fits, in particular for Cu/S(NO). The values of the fitted parameters are gathered in Table 2, together with the average fitting error, estimated as the maximum relative deviation between the fit and the data for $q \leq 0.06$ Å^{-1}. When analyzing

DOI: 10.1021/acs.jpcc.5b09556
J. Phys. Chem. C 2016, 120, 1488−1506

the fitting errors, it is useful to compare them with the fitting error of the empty SBA-15 in Figure 4, which is about 11%. Keeping that value in mind, it appears that an error of 9% for the correlated loading model is unrealistically small for Cu/S(NO). The apparent improvement in the quality of the fit is therefore likely to result merely from the extra degree of freedom available for the fit, rather than from a better structural accuracy of the model.

The partial conclusion of the present section is therefore that the uncorrelated mesopore-filling model describes successfully the metallic copper dispersion in samples Cu/S(N_2) and Cu(NO) at the mesoscopic scale. When correlation is allowed in the model the fitted values of the correlation length are close to 5 nm (see Table 2). Using that value in eq 34 with $d \simeq 11$ nm, corresponding to the distance between neighboring mesopores, the correlation between the filling of two neighboring mesopores is found to be as small as 0.13. Quite interestingly, the nitrate-loaded sample Cu/S can be fitted satisfactorily neither by the uncorrelated nor by the correlated mesopore-filling model, which hints at a qualitatively different spatial distribution of the loading among the pores.

Loading Model 2: Loading Patches. The inability of the mesopore-filling model to describe the SAXS of nitrate-loaded Cu/S sample motivated the development of the models presented in the current section. In theses models, we assume that the loading material comes in the form of patches that fill locally the pores (see Figure 6d). Qualitatively, the very existence of loading patches smaller than the grain would lead to a q^{-4} contribution to the scattering extending to large values of q. This is a central feature of the SAXS of Cu/S that the mesopore-filling model could not account for (see the insets of Figure 2a and Figure 7a).

The central ingredient of the patch model is the indicator function of the loading patches $L(\mathbf{x})$, illustrated in Figure 6d. We shall assume that $L(\mathbf{x})$ is statistically independent from all other structures, in particular from the meso- and micropores $m(\mathbf{x})$ and $\mu(\mathbf{x})$. In the case where the loading material would be allowed only in the mesopores, its indicator function would be written as $l(\mathbf{x}) = L(\mathbf{x})\, m(\mathbf{x})$. On the other hand, if the loading was allowed only in the micropores, we would have $l(\mathbf{x}) = L(\mathbf{x})\,[1 - m(\mathbf{x})]\mu(\mathbf{x})$. The general expression that we shall consider is therefore the following

$$l(\mathbf{x}) = L(\mathbf{x})\{\epsilon_1 m(\mathbf{x}) + \epsilon_2[1 - m(\mathbf{x})]\mu(\mathbf{x})\} \tag{39}$$

where ϵ_1 and ϵ_2 are parameters of the model, which can take the values 0 or 1 according to whether the model allows the loading in all pores ($\epsilon_1 = 1$ and $\epsilon_2 = 1$, see Figure 6e), only in the mesopores ($\epsilon_1 = 1$ and $\epsilon_2 = 0$, see Figure 6f), or only in the micropores ($\epsilon_1 = 0$ and $\epsilon_2 = 1$, see Figure 6g). In the following, we shall use the notation

$$\phi_p = \epsilon_1\phi_m + \epsilon_2[1 - \phi_m]\phi_\mu \tag{40}$$

for the volume fraction of all the pores that may receive some loading. This volume fraction is equal to ϕ_m, $(1 - \phi_m)\phi_\mu$ or $\phi_m + (1 - \phi_m)\phi_\mu$ depending on the values of ϵ_1 and ϵ_2.

Because the patches are statistically independent from the meso- and micropores, the volume fraction of the loading is calculated as $\phi_l = \phi_L\phi_p$. In order to calculate the electron correlation function $\chi_\rho(\mathbf{r})$ via eq 16, the correlation function of the loading $\chi_l(\mathbf{r})$ has to be calculated. Exploiting the statistical independence of $L(\mathbf{x})$, starting from eq 39 one finds the following expression

$$\chi_l(\mathbf{r}) = (\epsilon_1 - \epsilon_2\phi_\mu)^2\chi_m(\mathbf{r})(\chi_L(\mathbf{r}) + \phi_L^2) + \epsilon_2(1 - \phi_m)\phi_L\chi_\mu(\mathbf{r}) + \phi_p^2\chi_L(\mathbf{r}) \tag{41}$$

and the cross-correlation function defined by eq 14 is

$$\Gamma_{lm\mu}(\mathbf{r}) = \phi_L(1 - \phi_\mu)(\epsilon_1 - \epsilon_2\phi_\mu)\chi_m(\mathbf{r}) + \phi_L(1 - \phi_m)\epsilon_2\chi_\mu(\mathbf{r}) \tag{42}$$

For obtaining these equations, we have assumed that the micropores have a characteristic length much smaller than the patch function $L(\mathbf{x})$, so that approximations similar to eq 12 apply. Using these expressions in eq eq 16 leads to the following expression for the electron density correlation function

$$\begin{aligned}\frac{\chi_\rho(\mathbf{r})}{\theta_g} = {} & [(1 - \phi_m)(1 - \phi_\mu)\rho_s + \rho_l\phi_l]^2\Omega_g(\mathbf{r}) \\ & + [\rho_s(1 - \phi_\mu) - \rho_l\phi_L(\epsilon_1 - \epsilon_2\phi_\mu)]^2\chi_m(\mathbf{r})\Omega_g(\mathbf{r}) \\ & + V_g\rho_l^2(\epsilon_1 - \epsilon_2\phi_\mu)^2\chi_m(\mathbf{r})\chi_L(\mathbf{r}) + V_g(1 - \phi_m) \\ & [\rho_s^2(1 - \phi_L) + (\rho_s - \epsilon_2\rho_l)^2\phi_L]\chi_\mu(\mathbf{r}) \\ & + V_g\rho_l^2\phi_p^2\chi_L(\mathbf{r})\end{aligned} \tag{43}$$

The Fourier transform of this equation has to be calculated to estimate the intensity scattered by a structure such as Figure 6e–g.

The Fourier transform of every term in eq 43 corresponds to the scattering by a particular element of the overall hierarchical structure. The first and fourth terms correspond to the scattering by the grains as if they were homogeneous and by the micropores, respectively. The second term gives rise to a scattering term similar to the second line of eq 36 in the case of the mesopore-loading model: it accounts for the scattering by the mesopore structure with the square bracket being the relevant average contrast. The term on the third line is mathematically similar, only the corresponding structure factor has a different peak width, because it is determined by the characteristic size of the patches (via χ_L) rather than of the grains (via Ω_g); we shall write the latter structure factor as $Z'_L(\mathbf{q})$. The term on the last line is the scattering by the patches themselves. The final expression for the scattered intensity is the following

$$\begin{aligned}I(\mathbf{q}) = {} & [(1 - \phi_m)(1 - \phi_\mu)\rho_s + \rho_l\phi_l]^2\frac{2\pi A_g}{q^4} \\ & + N[\rho_s(1 - \phi_\mu) - \rho_l\phi_L(\epsilon_1 - \epsilon_2\phi_\mu)]^2 \\ & \{|\langle F(\mathbf{q})\rangle|^2[Z'(\mathbf{q}) - 1] + \langle|F(\mathbf{q})|^2\rangle\} \\ & + N\phi_L(1 - \phi_L)[(\epsilon_1 - \epsilon_2\phi_\mu)\rho_l]^2 \\ & \{|\langle F(\mathbf{q})\rangle|^2[Z'_L(\mathbf{q}) - 1] + \langle|F(\mathbf{q})|^2\rangle\} \\ & + V_g(1 - \phi_m)[\rho_s^2(1 - \phi_L) + (\rho_s - \epsilon_2\rho_l)^2\phi_L]I_\mu(\mathbf{q}) \\ & + V_g[\phi_p\rho_l]^2 I_L(\mathbf{q})\end{aligned} \tag{44}$$

where we have used the notation $I_L(q)$ for the Fourier transform of $\chi_L(\mathbf{r})$. Similar to our discussion of the mesopore-filling model eq 36 it is useful to think of the first four terms in eq 44 as of deformations of the SAXS of the empty material

DOI: 10.1021/acs.jpcc.5b09556
J. Phys. Chem. C 2016, 120, 1488–1506

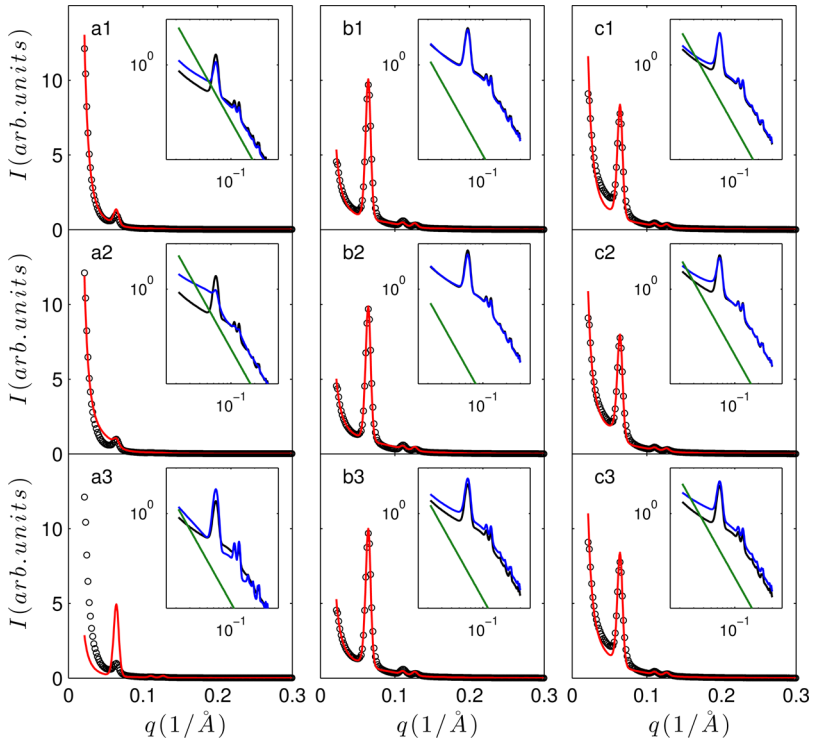

Figure 8. Fitting of the SAXS data of nitrate-loaded Cu/S (a1−a3) as well as of metal-loaded Cu/S(N2) (b1−b3) and Cu/S(NO) (c1−c3) with the patch model (model 2) corresponding to eq 44. The symbols are the data, and the solid red line is the least-squares fit with the all-pore filling ($\epsilon_1 = 1$ and $\epsilon_2 = 1$, top row), mesopore-filling ($\epsilon_1 = 1$ and $\epsilon_2 = 0$, middle row), and micropore-filling ($\epsilon_1 = 0$ and $\epsilon_2 = 1$, bottom row). The components of the best fits are shown in the insets on double logarithmic scales: scattering by the loading material itself (green) and by the porous support with contrast-matching corrections (blue). For comparison, the SAXS of the empty support is shown in black. In b1 and b2, the blue and black curves are indistinguishable at the scale of the figure, pointing at insignificant contrast-matching effects.

further to contrast matching corrections and to the last term as the additional scattering by the loading material itself.

In order to gain an intuitive understanding of eq 44 it is useful to analyze the corresponding integrated intensity in analogy with eq 4, as we did for the mesopore-filling model. The integrated intensity Q is obtained by evaluating $\chi_\rho(0)$ in eq 43, which leads to

$$\begin{aligned}\frac{Q}{(2\pi)^3\theta_g V_g} = {} & [(1-\phi_m)(1-\phi_\mu)\rho_s + \rho_l\phi_l]^2 \\ & + \{(1-\phi_L)[\rho_s(1-\phi_\mu)]^2 \\ & + \phi_L[\epsilon_1\rho_l - \epsilon_2\rho_l\phi_\mu - \rho_s(1-\phi_\mu)]^2\}\phi_m \\ & (1-\phi_m) + [\rho_l\phi_p]^2\phi_L(1-\phi_L) \\ & + (1-\phi_m)\{(1-\phi_L)[\rho_s]^2 \\ & + \phi_L[\rho_s - \epsilon_2\rho_l]^2\}\phi_\mu(1-\phi_\mu)\end{aligned} \tag{45}$$

In this expression, each term between square brackets is the electron density contrast relevant to a given region of space *at a given length scale*. The first term is similar to eq 38, and it corresponds to the scattering by the grain as a whole. The second term is the integrated intensity from both the second and third lines in eq 44: it corresponds to the scattering by the mesopore structure. That term is best viewed as the sum of the scattering by the mesopores falling outside and inside the loading patches, respectively. The former occupy the fraction $1 - \phi_L$ of space, and the electron density contrast is between 0 in the mesopores and $\rho_s\ (1 - \phi_\mu)$ in the complementary micropore region. The latter occupy the fraction ϕ_L of space, and the electron density there is between $\epsilon_1\ \rho_l$ in the loaded mesopores and $\epsilon_2\ \rho_l + (1 - \phi_\mu)\rho_s$ outside. The third term is the scattering by the patches themselves, seen as uniform regions with average electron density $\rho_l\phi_p + (1 - \phi_m)\ (1 - \phi_\mu)\rho_s$ contrasted with a background electron density $(1 - \phi_m)\ (1 - \phi_\mu)\rho_s$, corresponding to unloaded micro/mesoporous solid. The relevant contrast is therefore $\rho_l\phi_p$. Finally, the last term in eq 45 is the scattering from the micropore structure. It comprises the contributions of the regions inside and outside the patches, with weighting factors ϕ_L and $1 - \phi_L$. The terms between square brackets are the relevant electron density contrasts.

Before eq 44 can be used to fit the SAXS data, a specific model has to be chosen for the loading patch $L(\mathbf{x})$. In the case of the SAXS data of Cu/S, however, the actual model is not critical because only a q^{-4} Porod scattering is observed below $q \simeq 0.05$ Å^{-1} with no leveling off at lower values of q. This suggests that the characteristic length of the patches is larger than the lower resolution limit of the SAXS, so that a Porod approximation is sufficient for $I_L(q)$, namely

$$I_L(q) = \frac{2\pi S_L}{q^4} \tag{46}$$

where S_L is the surface area of the patches per unit volume of the entire material. This is mathematically identical to eq 18 used to account for the scattering of the grains.

For the scattering, the structure of the patches also intervenes via the structure factor $Z'_L(\mathbf{q})$, the width of the peaks of which is controlled by the size of the patches in the direction

DOI: 10.1021/acs.jpcc.5b09556
J. Phys. Chem. C 2016, 120, 1488−1506

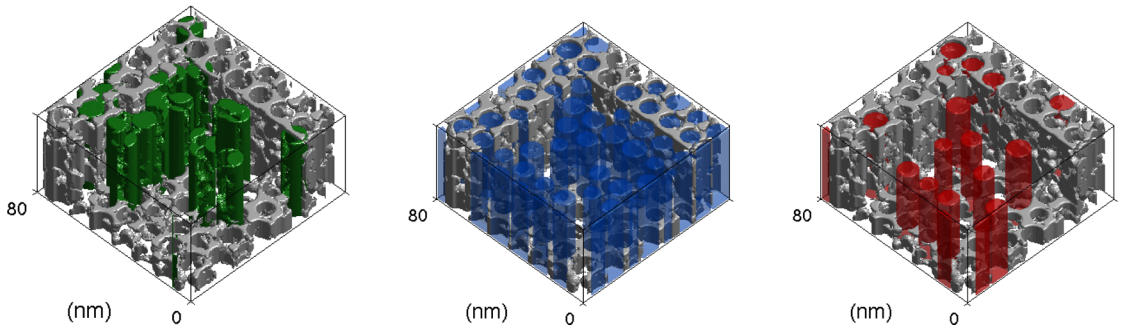

Figure 9. Realizations of the models that best describe the SAXS data of nitrate-loaded Cu/S (left, loading patches), as well as of metal-loaded Cu/S(N2) (middle, mesopore filling) and Cu/S(NO) (right, mesopore filling). In the latter two models, the transparency is a reminder that the mesopore-filling phase is not dense copper.

perpendicular to the mesopores. Based on Figure 1a, we shall assume that the loading patches have the same cylindrical symmetry as the mesopores, i.e., that the patch correlation function depends only on the distance orthogonal to the mesopores $\mathbf{r}_\perp$. Incidentally, that particular symmetry was implicit in Figure 6. The small-distance behavior of $\chi_L(\mathbf{r})$, relevant to the Porod scattering, has the following form

$$\chi_L(\mathbf{r}) = \phi_L(1-\phi_L)\left(1 - \frac{r_\perp}{l_C} + \cdots\right) \tag{47}$$

where l_C is the correlation length that is relevant to the size-broadening of $Z'_L(\mathbf{q})$. The corresponding structure factor can therefore be calculated as $Z'_g(\mathbf{q},l_C)$ using eq 53 of the Appendix. Moreover, the parameters l_C and S_L are not independent: given the cylindrical symmetry the two are related via[34,35]

$$S_L = \pi\frac{\phi_L(1-\phi_L)}{l_C} \tag{48}$$

Assuming statistically isotropic patches, rather than with a cylindrical symmetry, would result in the same expression with the factor π replaced by 4. Globally, the SAXS data can be analyzed with the patch models using ϕ_L and l_C as only fitting parameters.

The best fits of the SAXS data with the three patch models—all-pore loading ($\epsilon_1 = \epsilon_2 = 1$), mesopore loading ($\epsilon_1 = 1$, $\epsilon_2 = 0$), micropore loading ($\epsilon_1 = 0$, $\epsilon_2 = 1$)—are shown in Figure 8. The corresponding parameters of the model are gathered in Table 2. Because too small values of l_C would hardly be compatible with the observation of a Porod scattering pattern over the entire measured q-range, the correlation length l_C was not allowed to become smaller than 5 nm for the fit. The striking fact about Figure 8 is that the patch model with all-pore loading is the only one to describe accurately the SAXS of the nitrate-loaded sample Cu/S. Interestingly, the model proves inappropriate to describe the data if the nitrate is not allowed in the mesopores or in the micropores as testified by the large errors reported in Table 2. If nitrate is allowed in the mesopores only, the model cannot account for the scattering peak in the data due to a contrast-matching phenomenon (Figure 8a2). If nitrate is allowed in the micropores only, the model predicts a very strong peak due to a contrast-enhancement phenomenon. Moreover, the fit of the SAXS data leads to value of ϕ_l close to the lowest possible value. This suggests that the copper nitrate fills densely the pores. Finally, the relatively small value of l_C points to a rough surface of the nitrate patches.

Although the patch model was designed specifically for the nitrate-loaded sample Cu/S (with a q^{-4} background scattering) we also applied it to the metal-loaded samples Cu/S(N_2) and Cu/S(NO). Visually, the fits are reasonably good (see Figure 8b1−b3 and c1−c3), but the fitting errors are slightly larger than for the mesopore-filling model (see Table 2). It is interesting to note that the patch model with mesopore loading is equivalent to the mesopore-filling model, only with a very strong correlation. This is visible in Figure 6f, in which loaded mesopores are bound to form compact clusters. The larger errors resulting from using this model for Cu/S(N_2) and Cu/S(NO) therefore mean that correlation effects are extremely weak in the latter two metal-loaded samples.

Although it is beyond the scope of the present paper to analyze the mechanisms of formation of the different structures in Figure 9, it is interesting to imagine physicochemical mechanisms that would naturally lead to them. The starting point of the three materials is SBA-15 with all pores filled with a concentrated copper nitrate solution. Upon drying, the solution becomes progressively more concentrated (retracting menisci), and a heterogeneous nucleation process is to be expected, by which nitrate crystal nuclei would form on the silica surface. From a statistical point of view, those nuclei are likely to be located in the micropores, which hold most of the surface area. The confined growth of copper nitrate in porous silica has never been studied per se. In the case of cobalt nitrate, however, there is evidence that the crystals grow by invading progressively all the pore space available and engulfing the solid support.[61] Should this happen with copper nitrate too, it would naturally lead to the type of dense patch structure evidenced by SAXS. Based on what seems to be the case from microscopy (Figure 1) we assumed cylindrical patches aligned with the mesopores. The scattering data, however, can equally be fitted assuming statistically isotropic patches (not shown). This is done by replacing the factor π in eq 48 by a factor 4, which has marginal influence on the fits. Therefore, from the strict perspective of scattering the shape of the patches is unknown, but they are always found to extend over both micro- and mesopores.

The mechanisms involved during the subsequent heat treatment are better understood.[23] In the presence of NO, the nitrate decomposes into copper oxide via a $Cu_2(OH)_3(NO_3)$ intermediate species, which shows very little mobility hence preserving the nonuniform metal distribution obtained after drying. By contrast, under medium-to-high flow of pure N_2, decomposition of the copper nitrate into copper oxide happens with anhydrous $Cu(NO_3)_2$ as an intermediate

DOI: 10.1021/acs.jpcc.5b09556
J. Phys. Chem. C 2016, 120, 1488−1506

species, the high surface mobility of which is responsible for the well-nigh homogeneous spatial distribution of the copper species over the support. In both cases, the SAXS analysis suggests that the fraction of copper nitrate that was initially in the micropores is pushed into the mesopores when it is converted to copper oxide. Such a dewetting phenomenon is to be expected based on the much stronger interactions of copper nitrate with silica compared to copper oxide.[23]

DISCUSSION AND CONCLUSIONS

The main contribution of the present paper is the development of a general modeling methodology to analyze small-angle scattering patterns from hierarchical materials characterized by a variety of length scales. This was done mathematically by generalizing an approach introduced in earlier works,[16,21] namely by assuming that each structural level has a distinctive length scale and is statistically independent from the others. This leads to realistic structural models that are nevertheless mathematically simple enough to be of practical interest.

Small-angle scattering has often been used to analyze nanostructures with multiple scales, such as nanocomposites,[62] organic gels,[63] and porous materials,[64−66] among others. In most works, however, the contribution of each scattering level is described using Guinier or Porod empirical models,[67] with the prefactors considered as fitting parameters with no clear structural significance. The strength of our approach is that it enables one to produce comprehensive structural models that encompass all the relevant length scales of the material. This leads to mathematical expressions for the SAXS intensity with relatively few fitting parameters, all of which have a precise structural significance.

The complex combination of the various structural levels into the scattered intensity is well illustrated by the various expressions that we have obtained for the integrated intensity Q. All contributions to eqs 17, 38, and 45 can be intuitively understood in terms of the classical expression $(\rho_A - \rho_B)^2\phi_A\phi_B$, applied to specific regions of the materials *at specific length scales*. The same type of expressions were obtained for the integrated intensity scattered by semicrystalline polymers;[68] our approach enables one to derive these intuitive expressions in a systematic and mathematically rigorous way.

We have illustrated our general data analysis methodology with the SAXS of copper-loaded SBA-15 ordered mesoporous silica. For that purpose, we have developed a comprehensive model of the SBA-15 structure, accounting for the mesoporosity, for the microporosity, as well as for the large-scale grain structure of the material. That model is best summed up by the particular realization shown in Figure 5. Because every parameter in the model has a precise structural significance, we incorporate in the scattering data analysis independent structural information on the material. In particular, our model of SBA-15 is in quantitative agreement with the experimental SAXS pattern as well as with the specific surface area and mesopore volume measured by nitrogen adsorption.

We then generalized the model to allow some loading materials into the pores, in order to analyze the spatial distribution of copper nitrate as well as of metallic copper in two supported catalysts. Our approach enabled us to discriminate the situations in which the loading is present only in the mesopores (the metallic copper in sample Cu/S(N_2) and Cu/S(NO)) or both in the meso- and micropores (the copper nitrate in sample Cu/S). Moreover, the modeling of the SAXS data predicts that the distribution of the metal in the mesopores in more homogeneous in the catalyst heat-treated in nitrogen flow, in perfect agreement with earlier electron tomography work.[21] The overall results of the SAXS analysis of is summed up by Figure 9. These are realizations of the models that best fit the SAXS data.

Figure 9 displays particular realizations of the models used to fit the SAXS data, which should not be confused with the models themselves. In our probabilistic approach, the models are defined by the statistical rules used to generate the structure. For example, in the case of the mesoporore-filling model one such rule consisted in filling randomly each mesopore with a given probability $\langle\Lambda\rangle$. It has to be stressed that the mathematical expressions that we have derived for the SAXS intensity (e.g., eq 36 and eq 44) capture both the average structure and the structure variability within the entire volume of material probed by the X-rays. In that respect, it is useful to remind that a typical amount of material sampled by a SAXS experiment is 10^{-3} g, while while the approximate mass of the volumes shown in Figure 9 is 10^{-15} g. The use of a probabilistic approach is therefore central to bridge the 12-decade sampling gap between the macroscopic scattering experiment and the nanometer-scale structure of the materials.

The present work has ramifications beyond the study of active phase dispersion in supported catalysts; it is in principle relevant to any small-angle scattering study on porous materials for which mesoscopic-scale heterogeneity may play a role. A few examples among many others are the stability of ordered mesoporous materials, which become heterogeneous during hydrothermal treatment,[69] the SAXS characterization of porous nanocomposites,[70] one component of which can be treated formally as if it were a loading phase, and naturally the study of confined phase equilibria. In the latter field in particular, most in situ scattering studies of adsorption in SBA-15 assume a single density profile that applies to all mesopores.[15,71−73] In a few studies, the variability of the filling from one mesopore to the next is analyzed.[60] The authors are not aware of any scattering work analyzing the variability of the filling along the mesopores, which would be needed to analyze such important effects as capillary bridge formation and cavitation.[45] Although the specific models used in the present work also assume homogeneous structures along the mesopores, the general correlation function eq 16 can be particularised to models suitable for that type of studies.

The models can also be generalized to other types of porous materials. Equations 36 and 44 hold true for other types of ordered mesoporous materials, besides SBA-15. In the case of, say SBA-16,[74] $Z(\mathbf{q})$ would have to be replaced by the structure factor of a cubic lattice and $F(\mathbf{q})$ by the form factor of spherical pores, but the general expression of the SAXS intensity would remain valid. Moreover, it is interesting to note that the upper and lower pore size limits of mesopores (50 and 2 nm according to IUPAC[31]) incidentally coincide with the upper and lower resolution limits of most SAXS experiments. Therefore, the Porod and Guinier approximations for the scattering by large-scale (eq 18) and small-scale (eq 19) structures are expected to be applicable to the SAXS analysis of a wide array of micro/meso/macroporous materials.

Finally, the ramifications of our work extend beyond porous materials. Materials with hierarchical structures in the nanometer range are extremely common in biological settings[75] and also in synthetic polymers.[76] The general methods that we have introduced, assuming that each structural level has a distinct characteristic scale and is statistically independent from the

DOI: 10.1021/acs.jpcc.5b09556
J. Phys. Chem. C 2016, 120, 1488−1506

others, can in principle be applied to the SAXS analysis of any hierarchical structure. Another field of application would be the joint analysis of small-angle and wide-angle scattering scattering patterns (SAXS/WAXS). It is, in principle, possible with our general approach to produce practical mathematical models to perform a SAXS-like analysis of the shape of crystallographic Bragg peaks.[77] We hope that the present work will help researchers interested in all those fields take full advantage of the rich structural information contained in small-angle scattering data.

APPENDIX

Structure Factors of the 2D Hexagonal Lattice

There is some confusion in the literature about the absolute value of the lattice factor $Z(\mathbf{q})$ for 2D hexagonal lattices. In most cases, this is not problematic because it is used to analyze only the relative values of the various scattering peaks.[26,40,48,65,71,73,78,79] However, In the present case the structural information about the spatial distribution of the confined material lies entirely in the relative intensities of various contributions to the small-angle scattering. It is therefore important to use the accurate absolute value of the lattice factor.

We shall start here with the generalized definition of the lattice factor given by eq 37. The equation can be written equivalently as

$$Z_g(\mathbf{q}) = \sum_n g(d_n) e^{-i\mathbf{q}\cdot\mathbf{d}_n} \tag{49}$$

where the sum is over all the possible vectorial distances between the points of the hexagonal lattice, including $\mathbf{d} = 0$. Because the 2D hexagonal lattice lies in a plane, the structure factor only depends on the 2D projection of the 3D scattering vector, which we called $\mathbf{q}_\perp$ in the main text. Unless specified differently, the vector $\mathbf{q}$ has strictly to be understood in the present appendix as $\mathbf{q}_\perp$, and q as $|\mathbf{q}_\perp|$.

Although we shall eventually assumes an exponential form for the function $g(d)$, we assume for now that it is any 2D integrable radial function. Equation 49 can be understood as the 2D Fourier transform of the product of two factors, namely the function $g(d)$ and an infinite sum of Dirac functions. Using the 2D convolution theorem, $Z_g(q)$ can therefore be written as

$$Z_g(\mathbf{q}) = \frac{2}{\sqrt{3}a^2} G(q) + \frac{2}{\sqrt{3}a^2} \sum_{hk} G(|\mathbf{q} - \mathbf{q}_{hk}|) \tag{50}$$

where $G(q)$ is the Fourier transform of $g(d)$, the sum is now over the nodes of the reciprocal lattice (referred to via their Miller indices hk), and the factor $\sqrt{3a^2/2}$ is the area of a hexagonal unit cell in real space.

Because we are eventually interested in fitting powder scattering patterns, $Z_g(\mathbf{q})$ has to be averaged over all possible orientations of the hexagonal lattice. The situation is sketched in Figure 10: the averaging is equivalent to the following integration over a circle or radius q centered on the origin

$$Z_g(q) = \frac{2}{\sqrt{3}a^2} G(q) + \frac{2}{\sqrt{3}a^2} \sum_{hk} \frac{1}{2\pi q} \int_{\text{circle } q} G(|\mathbf{q} - \mathbf{q}_{hk}|) d\mathbf{q} \tag{51}$$

where the factor $2\pi q$ is the perimeter of the circle. Although the calculation presents no conceptual difficulty it does not lead to any closed analytical form. We therefore adopted the simplification shown in Figure 10, whereby the circle integration is approximated by a line integration. This approximation is legitimate whenever $G(|\mathbf{q} - \mathbf{q}_{hk}|)$ is a function that decreases sufficiently rapidly toward 0.

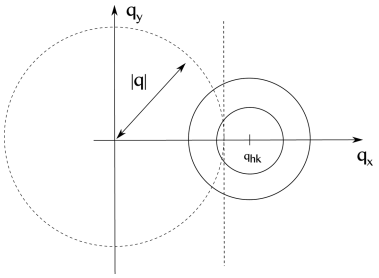

Figure 10. Sketch of the rotation average calculation in reciprocal space: the solid circles are iso-value lines of $G(|\mathbf{q} - \mathbf{q}_{hk}|)$ where only one node of the reciprocal lattice is shown. The rotation average is equivalent to integrating that function over the dashed circle. The calculation may be approximated by the integration over the dashed line, provided $G \simeq 0$ wherever the line and the circle are far away from each other.

In the case of an exponential function of the type of eq 34, $g(d) = \exp(-d/l_C)$, the 2D Fourier transform is

$$G(q) = \frac{2\pi l_C^2}{[1 + (q l_C)^2]^{3/2}} \tag{52}$$

Using that expression in eq 51 and approximating the circle integration by the line integration eventually leads to

$$Z_g(q, l_C) = \frac{4\pi}{\sqrt{3}} \left(\frac{l_C}{a}\right)^2 [1 + (q l_C)^2]^{-3/2} + \frac{4\pi}{\sqrt{3}a^2} \sum_{hk} \frac{m_{hk}}{q} \frac{l_C}{\pi} [1 + l_C^2 (q - q_{hk})^2]^{-1} \tag{53}$$

where m_{hk} is the multiplicity of the scattering peak at q_{hk}. For the hexagonal lattice, the positions q_{hk} and multiplicities m_{hk} of the peaks are given by[26,27]

$$q_{hk} = \frac{4\pi}{a\sqrt{3}} \sqrt{h^2 + k^2 + hk} \tag{54}$$

with integer values of h and k, and the corresponding multiplicities are

$$m_{hk} = \begin{cases} 6 & \text{for all h and } k = 0 \\ 6 & \text{for } h = k \\ 12 & \text{for } h \neq k \end{cases} \tag{55}$$

Figure 11 shows that eq 53 is very accurate, even for values of l_C as low as $a/2$, for which the accuracy of the line-integration approximation was not guaranteed. For low values of l_C/a, however, the tails of the first scattering peak extend so far as the origin of q. In that case, the factor $1/q$ in eq 53 leads to a spurious divergence of $Z_g(q)$. This situation can be improved by replacing the factor $1/q$ by $1/q_{hk}$. This was done for the values plotted in Figure 11.

Equation 53 shows that the shape of the scattering peaks is exactly a Lorentzian in the case of an exponential $g(d)$. However, it is often desirable to use a more general function to describe the scattering peaks. Replacing the normalized

DOI: 10.1021/acs.jpcc.5b09556
J. Phys. Chem. C 2016, 120, 1488−1506

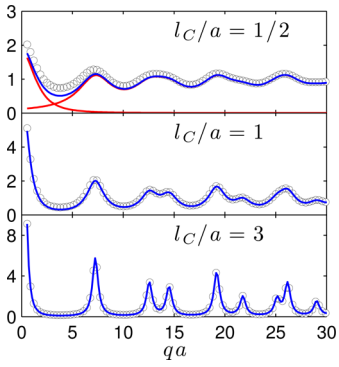

Figure 11. Structure factor $Z_g(q,l_C)$ for various values of l_C/a. The dots are the direct evaluation of eq 49 and the blue line is eq 53. In the case of $l_C/a = 1/2$ the central component of the scattering is shown in red, together with the lattice factor Z'_g from which the central scattering has been subtracted.

Lorentzian by another normalized peaked function $L()$ leads to the following expression

$$Z'(q) = \frac{4\pi}{\sqrt{3}\,a^2} \sum_{hk} \frac{m_{hk}}{q} L(q - q_{hk}) \tag{56}$$

In the main text, we used the same function $L()$ as Förster et al.,[27] which has two parameters ν and δ controlling the shape of the peaks (from Lorentzian to Gaussian) and their width, respectively. Another popular choice is the pseudo-Voigt function, equal to a weighted sum of a Lorentzian and a Gaussian.

For the purpose of fitting experimental data, some disorder is introduced in the lattice via a Debye–Waller procedure,[38,56] which results in the following substitution

$$Z(q) \rightarrow (Z(q) - 1)e^{-1/2(\sigma_a q)^2} + 1 \tag{57}$$

where σ_a is the random deviation of each lattice point from its ideal position.

It has to be stressed that the factor $4\pi/(\sqrt{3}a^2)$ in eq 56 differs from values found in the literature. In particular, it is larger than the value used by Sundblom et al.[80] by a factor as large as 2π. It is also unclear what space dimension has to be used in eq 23 of the paper of Förster et al.[27] to recover eq 56. In addition to being a direct consequence of the definition of $Z_g(q)$ through eq 53, the value of the prefactor in eq 56 can also be justified by the requirement that $Z(q)$ should converge to 1 for large values of q. This can be written more accurately as

$$\lim_{q\to\infty} \frac{1}{dq} \int_q^{q+dq} Z(q)\mathrm{d}q = 1 \tag{58}$$

for infinitesimally small values of dq. The integral between q and $q + dq$ of the sum in eq 56 is equal to the number of nodes of the reciprocal lattice in a ring of area $2\ \pi\ q\ dq$, which converges therefore to

$$2\pi\mathrm{q}\mathrm{d}\mathrm{q}/\left[\frac{(2\pi)^2}{a^2\sqrt{3}/2}\right] \tag{59}$$

for large values of q, where the term between brackets is the area of the reciprocal unit cell of the hexagonal lattice.[27,53] From that value, it is apparent that the factor used in eq 56 is indeed correct if eq 58 is to be satisfied.

Simplified Orientation-Averaging Procedure

In order to use mathematical expressions like eq 24 or eq 26 to analyze powder scattering patterns, their average value has to be calculated, over all possible orientations of the grain. The averaging procedure can be significantly simplified in the case where the height H of the pores (identical to the height of the grain) is much larger than their lateral dimensions. In this case all the scattered intensity takes non-vanishing values only within a thin layer in reciprocal space centred on $q_z = 0$ with thickness of the order of $1/H$, and they have azimuthal symmetry in that plane. If we write $c(q_\perp,q_z)$ any function having that type of cylindrical symmetry, its orientation average $\bar{c}\ (q)$ can be approximated as

$$\bar{c}(q) = \frac{\alpha}{2qH} c(q_\perp = q,\ q_z = 0) \tag{60}$$

where α is a numerical factor that has yet to be specified. Equation(60) comes from the observation that $\bar{c}\ (q)$ is the average value of $c(q_\perp,\ q_z)$ on the surface of a sphere in reciprocal space centred on the origin with radius q. The fraction of the surface of the sphere that is within the $1/H$-thick layer is $1/(2q\mathrm{H})$; in that region the value of c is close to $c(q_\perp = q,q_z = 0)$ and it vanishes elsewhere.

We introduced the yet unknown factor α to make the averaging rule eq 60 more accurate. It seems legitimate to chose for α the particular value that preserves exactly the integrated intensity Q in the particular case where $c(\mathbf{q}) = |F(\mathbf{q})|^2$, with $F()$ given by eq 26. It results from the definition of $F()$ as the Fourier transform of a cylinder, and from Parseval's theorem that

$$\int F^2(\mathbf{q})dV_q = (2\pi)^3\pi R^2 H \tag{61}$$

where $\pi\ R^2H$ is the volume of the cylinder. Imposing that the integral of the rotationally averaged quantity $\int_0^\infty \overline{F^2}\ (q)\ 4\ \pi\ q^2\ dq$ takes the same value, one finds that the adequate value is $\alpha = 2\pi$. This is the value that we use in the rest of the paper. In other words, the rotational average is done by setting $\mathbf{q}_z = 0$, replacing $\mathbf{q}_\perp$ by $q = |\mathbf{q}|$ and by multiplying the term by $\pi/(q\ H)$.

Volume Fraction and Surface Area of Boolean Models

Models of penetrable spheres are used on several instances in the main text, notably to generate the realisations of the microporous structure of SBA-15 in Figure 5 and of the nitrate patches in Figure 9. Models of fully penetrable spheres are also referred to as Boolean models in more mathematically-oriented literature. Many of their statistical properties have been known for a long time,[34,37,81,82] and they serve as building blocks for more elaborate models of random structures.[33] We recall here the theoretical results needed to generate the realisations of penetrable-sphere model based on their volume fraction ϕ_s and surface area S_s.

The two-point correlation function of the 3D penetrable spheres (of 2D penetrable disks) with radius R is calculated using the general formulae of Boolean models as[34,37]

$$P_{ss}(r) = 2\phi_s - 1 + (1 - \phi_s)^2 e^{\theta_s\Omega_s(r)} \tag{62}$$

where θ_s is the density of the underlying Poisson point process, corresponding to the average number of spheres per unit volume (disks per unit area), and $\Omega_s(r)$ is the autocorrelation function of the spheres (of the disks). The two-point function $P_{ss}(r)$ has the same meaning as in eq 9: it is the probability that two points at a distance r from one another are both inside a

DOI: 10.1021/acs.jpcc.5b09556
J. Phys. Chem. C 2016, 120, 1488−1506

sphere (independently of whether it is the same sphere or two distinct spheres).

The function $\Omega_s(r)$ is the volume (area) of the intersection of two identical spheres (disks) the centres of which are at a distance r from one another. For 3D spheres of radius R, the function is

$$\Omega_s(r) = \frac{2\pi}{3}R^3\left(1 - \frac{r}{2R}\right)^2\left(2 + \frac{r}{2R}\right) \quad (63)$$

for $r \leq 2R$, and 0 otherwise. For 2D disks, the value is

$$\Omega_s(r) = 2R^2\left\{\cos^{-1}\left(\frac{r}{2R}\right) - \frac{r}{2R}\sqrt{1 - \left(\frac{r}{2R}\right)^2}\right\} \quad (64)$$

for $r \leq 2R$, and 0 otherwise.

The volume fraction is obtained as $\phi_s = P_{ss}(0)$, and the surface area is obtained from the derivative of $P_{ss}(r)$ as

$$S_s = \alpha\left[\frac{dP_{ss}}{dr}\right]_{r=0} \quad (65)$$

where $\alpha = 4$ or $\alpha = \pi$ for 3D and 2D structures, respectively.[28,34,35] In the case spheres, the volume fraction and surface area are given by

$$\phi_s = 1 - \exp\left(-\theta_s\frac{4\pi}{3}R^3\right)$$
$$S_s = \exp\left(-\theta_s\frac{4\pi}{3}R^3\right)\theta_s 4\pi R^2 \quad (66)$$

Note that in the limit of low density (for $\theta_s \to 0$) these expression converge to $\phi_s \to \theta_s\, 4/3\, \pi\, R^3$ and $S_s \to \theta_s\, 4\, \pi\, R^2$, as expected if the overlapping of spheres is negligible. In the case of disks, the result is

$$\phi_s = 1 - \exp(-\theta_s\pi R^2)$$
$$S_s = \exp(-\theta_s\pi R^2)\theta_s 2\pi R \quad (67)$$

Equations 66 and 67 can be inverted to find the density θ_s and the radius R of spheres (disks) corresponding to any given volume fraction ϕ_s and specific surface area S_s. This is how the realizations in Figures 5 and 9 were obtained.

AUTHOR INFORMATION

Corresponding Author

*E-mail: cedric.gommes@ulg.ac.be.

Present Address

§(G.P.) Heterogeneous Catalysis, Max-Planck-Institut für Kohlenforschung Kaiser-Wilhelm-Platz 1, D-45470 Mülheim an der Ruhr, Germany.

Notes

The authors declare no competing financial interest.

ACKNOWLEDGMENTS

CJG is a Research Associate at the Funds for Scientific Research (F.R.S.-FNRS, Belgium). Part of this work was done during a stay of CJG in the Department of Inorganic Chemistry and Catalysis in Utrecht, supported by the Patrimoine de L'Université de Liège; it is a pleasure to acknowledge stimulating discussions with Dr. Jovana Zecevic and Prof. Krijn de Jong. The authors are also grateful to Ms. Maja Vanhalle and to Prof. Bart Goderis (KULeuven, Belgium) for measuring the SAXS patterns and for reading the first draft of the manuscript.

REFERENCES

(1) Taguchi, A.; Schüth, F. Ordered mesoporous materials in catalysis. *Microporous Mesoporous Mater.* **2005**, *77*, 1−45.

(2) Schoonheydt, R. A.; Weckhuysen, B. M. Editorial highlight: molecules in confined spaces. *Phys. Chem. Chem. Phys.* **2009**, *11*, 2794−2798.

(3) Ruthven, D. M.; Reyes, S. C. Adsorptive separation of light olefins from paraffins. *Microporous Mesoporous Mater.* **2007**, *104*, 59−66.

(4) Holby, E. F.; Sheng, W.; Shao-Horn, Y.; Morgan, D. Pt nanoparticle stability in PEM fuel cells: influence of particle size distribution and crossover hydrogen. *Energy Environ. Sci.* **2009**, *2*, 865−871.

(5) De Jongh, P. E.; Adelhelm, P. Nanosizing and nanoconfinement: New strategies towards meeting hydrogen storage goals. *ChemSusChem* **2010**, *3*, 1332−1348.

(6) Antolini, E. Carbon supports for low-temperature fuel cell catalysts. *Appl. Catal., B* **2009**, *88*, 1−24.

(7) Coussy, O. Deformation and stress from in-pore drying-induced crystallization of salt. *J. Mech. Phys. Solids* **2006**, *54*, 1517−1547.

(8) Fujiyoshi, Y.; Murata, K.; Mitsuoka, K.; Hiral, T.; Walz, T.; Agre, P.; Heymann, J. B.; Engel, A. Structural determinants of water permeation through aquaporin-1. *Nature* **2000**, *407*, 599−605.

(9) Friedrich, H.; de Jongh, P. E.; Verkleij, A.; de Jong, K. P. Electron tomography for heterogeneous catalysts and related nano materials. *Chem. Rev.* **2009**, *109*, 1613−1629.

(10) Midgley, P.; Dunin-Borkowski, R. E. Electron tomography and holography in materials science. *Nat. Mater.* **2009**, *8*, 271−280.

(11) Glatter, O.; Kratky, O. *Small Angle X-ray Scattering*; Academic Press: New York, 1982.

(12) Sivia, D. S. *Elementary Scattering Theory*; Oxford University Press: Oxford, 2011.

(13) Juanhuix, J.; Bordas, J.; Campmany, J.; Svensson, A.; Bassford, M.; Narayanan, T. Axial disposition of myosin heads in isometrically contracting muscles. *Biophys. J.* **2001**, *80*, 1429−1441.

(14) Nogales, A.; Hsiao, B.; Somani, R. H.; Srinivas, S.; Tsou, A. H.; Balta-Calleja, F. J.; Ezquerra, T. A. Shear-induced crystallization of isotactic polypropylene with different molecular weight distributions: in situ small- and wide-angle x-ray scattering studies. *Polymer* **2001**, *42*, 5247−5256.

(15) Hofmann, T.; Wallacher, D.; Huber, P.; Birringer, R.; Knorr, K.; Schreiber, A.; Findenegg, G. H. Small-angle x-ray diffraction of Kr in mesoporous silica: effects of microporosity and surface roughness. *Phys. Rev. B: Condens. Matter Mater. Phys.* **2005**, DOI: 10.1103/PhysRevB.72.064122.

(16) Gommes, C. J.; Roberts, A. P. Structure development of resorcinol-formaldehyde gels: microphase separation or colloid aggregation. *Phys. Rev. E* **2008**, *77*, 041409.

(17) Podsiadlo, P.; Lee, B.; Prakapenka, V. B.; Krylova, G. V.; Schaller, R. D.; Demortiére, A.; Shevchenko, E. V. High-pressure structural stability and elasticity of supercrystals self-assembled from nanocrystals. *Nano Lett.* **2011**, *11*, 579−588.

(18) Ciccariello, S.; Melnichenko, Y. B.; He, L. Phase behavior of carbon dioxide confined in silica aerogel in the vicinity of the bulk critical point. *J. Phys. Chem. C* **2011**, *115*, 22336−22346.

(19) Meir, Y.; Jerby, E.; Barkay, Z.; Ashkenazi, D.; Mitchell, J. B.; Narayanan, T.; Eliaz, N.; LeGarrec, J. L.; Sztucki, M.; Meshcheryakov, O. Observations of ball-lightning-like plasmoids ejected from silicon by localized microwaves. *Materials* **2013**, *6*, 4011−4030.

(20) Henzler, K.; Rosenfeldt, S.; Wittemann, A.; Harnau, L.; Finet, S.; Narayanan, T.; Ballauff, M. Directed motion of proteins along tethered polyelectrolytes. *Phys. Rev. Lett.* **2008**, DOI: 10.1103/PhysRevLett.100.158301.

(21) Gommes, C. J.; Prieto, G.; Zecevic, J.; Vanhalle, M.; Goderis, B.; de Jong, K. P.; de Jongh, P. E. Mesoscale characterization of

DOI: 10.1021/acs.jpcc.5b09556
J. Phys. Chem. C 2016, 120, 1488−1506

nanoparticles distribution using x-ray scattering. *Angew. Chem., Int. Ed.* **2015**, *54*, 11804−11808.
(22) Beck, J. S.; Vartuli, J. C.; Roth, W. J.; Leonowicz, M. E.; Kresge, C. T.; Schmitt, K. D.; Chu, C. T.; Olson, D. H.; Sheppard, E. W.; McCullen, S. B.; et al. A new family of mesoporous molecular sieves prepared with liquid crystal templates. *J. Am. Chem. Soc.* **1992**, *114*, 10834−10843.
(23) Munnik, P.; Wolters, M.; Gabrielsson, A.; Pollington, S. D.; Headdock, G.; Bitter, J. H.; De Jongh, P. E.; De Jong, K. P. Copper nitrate redispersion to arrive at highly active silica-supported copper catalysts. *J. Phys. Chem. C* **2011**, *115*, 14698−14706.
(24) Prieto, G.; Zecevic, J.; Friedrich, H.; De Jong, K. P.; De Jongh, P. E. Towards stable catalysts by controlling collective properties of supported metal nanoparticles. *Nat. Mater.* **2012**, *12*, 34.
(25) Gommes, C. J.; Goderis, B. CONEX, a program for angular calibration and averaging of two-dimensional powder scattering patterns. *J. Appl. Crystallogr.* **2010**, *43*, 352−355.
(26) Imperor-Clerc, M.; Davidson, P.; Davidson, A. Existence of a microporous corona around the mesopores of silica-based SBA-15 materials templated by triblock copolymers. *J. Am. Chem. Soc.* **2000**, *122*, 11925−11933.
(27) Förster, S.; Timmann, A.; Konrad, M.; Schellbach, C.; Meyer, A.; Funari, S. S.; Mulvaney, P.; Knott, R. Scattering curves of ordered mesoscopic materials. *J. Phys. Chem. B* **2005**, *109*, 1347−1360.
(28) Debye, P.; Anderson, H. R.; Brumberger, H. Scattering by an inhomogeneous solid 2. The correlation function and its application. *J. Appl. Phys.* **1957**, *28*, 679−683.
(29) Feigin, L. A.; Svergun, D. I. *Structure Analysis by Small-Angle X-Ray and Neutron Scattering*; Springer: Berlin, 1987.
(30) Ciccariello, S.; Cocco, G.; Benedetti, A.; Enzo, S. Correlation functions of amorphous multiphase systems. *Phys. Rev. B: Condens. Matter Mater. Phys.* **1981**, *23*, 6474−6485.
(31) Rouquerol, J.; Avnir, D.; Fairbridge, C. W.; Everett, D. H.; Haynes, J. H.; Pernicone, N.; Ramsay, J. D. F.; Sing, K. S. W.; Unger, K. K. Recommendations for the characterisation of porous solids. *Pure Appl. Chem.* **1994**, *66*, 1739−1758.
(32) Matheron, G. *Éléments pour une Théorie des Milieux Poreux*; Masson: Paris, 1967.
(33) Jeulin, D. Random texture models for material structures. *Stat. Comput.* **2000**, *10*, 121−132.
(34) Serra, J. *Image Analysis and Mathematical Morphology*; Academic Press: London, 1982; Vol. *1*.
(35) Torquato, S. *Random Heterogeneous Materials*; Springer: New York, 2000.
(36) Frisch, H. L.; Stillinger, F. H. Contribution to the statistical geometric basis of radiation scattering. *J. Chem. Phys.* **1963**, *38*, 2200−2207.
(37) Sonntag, U.; Stoyan, D.; Hermann, H. Random set models in the interpretation of small-angle scattering data. *Phys. Stat. Sol. A* **1981**, *68*, 281−288.
(38) Guinier, A. *X-Ray Diffraction*; Freeman: San Francisco, 1963.
(39) Ciesla, U.; Schüth, F. Ordered mesoporous materials. *Microporous Mesoporous Mater.* **1999**, *27*, 131−149.
(40) Gommes, C. J.; Friedrich, H.; Wolters, M.; De Jongh, P. E.; De Jong, K. P. Quantitative characterization of pore corrugation in ordered mesoporous materials using image analysis of electron tomograms. *Chem. Mater.* **2009**, *21*, 1311−1317.
(41) Galarneau, A.; Cambon, H.; Di Renzo, F.; Fajula, F. True microporosity and surface area of mesoporous SBA-15 silicas as a function of synthesis temperature. *Langmuir* **2001**, *17*, 8328−8335.
(42) Prass, J.; Müter, D.; Fratzl, P.; Paris, O. Capillarity-driven deformation of ordered nanoporous silica. *Appl. Phys. Lett.* **2009**, *95*, 083121.
(43) Gommes, C. J.; Friedrich, H.; de Jongh, P. E.; de Jong, K. P. Two-point correlation function of nanostructured materials via the grey-tone correlation function of electron tomograms: a three-dimensional structural analysis of ordered mesoporous silica. *Acta Mater.* **2010**, *58*, 770−780.
(44) Gommes, C. J.; Pirard, J. P. Morphological models of complex ordered materials based on inhomogeneously clipped Gaussian fields. *Phys. Rev. E* **2009**, *80*, 061401.
(45) Gommes, C. J. Adsorption, capillary bridge formation, and cavitation in SBA-15 corrugated mesopores: a Derjaguin-Broekhoff-de Boer analysis. *Langmuir* **2012**, *28*, 5101−5115.
(46) Jähnert, S.; Müter, D.; Prass, J.; Zickler, G. A.; Paris, O.; Findenegg, G. H. Pore structure and fluid sorption in ordered mesoporous silica. I. Experimental study by in situ small-angle x-ray scattering. *J. Phys. Chem. C* **2009**, *113*, 15201−15210.
(47) Müter, D.; Jähnert, S.; Prass, J.; Zickler, G. A.; Paris, O.; Findenegg, G. H. Pore structure and fluid sorption in ordered mesoporous silica. II. Modeling. *J. Phys. Chem. C* **2009**, *113*, 15211−15217.
(48) Findenegg, G. H.; Jähnert, S.; Müter, D.; Prass, J.; Paris, O. Fluid adsorption in ordered mesoporous solids determined by in situ small-angle X-ray scattering. *Phys. Chem. Chem. Phys.* **2010**, *12*, 7211−7220.
(49) Cambedouzou, J.; Diat, O. Quantitative small-angle scattering on mesoporous silica powders: from morphological features to specific surface estimation. *J. Appl. Crystallogr.* **2012**, *45*, 662−673.
(50) Ciccariello, S.; Goodisman, J.; Brumberger, H. On the Porod law. *J. Appl. Crystallogr.* **1988**, *21*, 117−128.
(51) Hammouda, B. A new Guinier-Porod model. *J. Appl. Crystallogr.* **2010**, *43*, 716−719.
(52) Mering, J.; Tchoubar, D. Interpretation de la diffusion centrale des rayons x par les systèmes poreux. I. *J. Appl. Crystallogr.* **1968**, *1*, 153−165.
(53) Förster, S.; Fischer, S.; Zielske, K.; Schellbach, C.; Sztucki, M.; Lindner, P.; Perlich, J. Calculation of scattering-patterns of ordered nano- and mesoscale materials. *Adv. Colloid Interface Sci.* **2011**, *163*, 53−83.
(54) Pedersen, J. S. Analysis of small-angle scattering data from colloids and polymer solutions: modeling and least-squares fitting. *Adv. Colloid Interface Sci.* **1997**, *70*, 171−210.
(55) Ehrburger-Dolle, F.; Morfin, I.; Geissler, E.; Bley, F.; Livet, F.; Vix-Guterl, C.; Saadallah, S.; Parmentier, J.; Reda, M.; Patarin, J.; et al. Small-angle x-ray scattering and electron microscopy investigation of silica and carbon replicas with ordered porosity. *Langmuir* **2003**, *19*, 4303−4308.
(56) Kittel, C. *Introduction to Solid State Physics*, 8th ed.; Wiley: New York, 2003.
(57) Ravikovitch, P. I.; Neimark, A. V. Density functional theory model of adsorption on amorphous and microporous silica materials. *Langmuir* **2006**, *22*, 11171−11179.
(58) Yuan, P.; Tan, L.; Pan, D.; Guo, Y.; Zhou, L.; Yang, J.; Zou, J.; Yu, C. A systematic study of long-range ordered 3D-SBA-15 materials by electron tomography. *New J. Chem.* **2011**, *35*, 2456−2461.
(59) Gommes, C. J.; Pirard, J. P.; Goderis, B. Condensation-induced decrease of small-angle x-ray scattering intensity in gelling silica solutions. *J. Phys. Chem. C* **2010**, *114*, 17350−17357.
(60) Erko, M.; Wallacher, D.; Brandt, A.; Paris, O. In-situ small-angle neutron scattering study of pore filling and pore emptying in ordered mesoporous silica. *J. Appl. Crystallogr.* **2010**, *43*, 1−7.
(61) Munnik, P.; De Jongh, P. E.; De Jong, K. P. Control and impact of the nanoscale distribution of supported cobalt particles used in Fischer−Tropsch catalysis. *J. Am. Chem. Soc.* **2014**, *136*, 7333−7340.
(62) Millan, A.; Urtizberea, A.; Silva, N. J. D. O.; Boesecke, P.; Natividad, E.; Palacio, F.; Snoeck, E.; Soriano, L.; Gutiérrez, A.; Quirós, C. Multiple-length-scale small-angle x-ray scattering analysis on maghemite nanocomposites. *J. Appl. Crystallogr.* **2007**, *40*, s696−s700.
(63) Chalal, M.; Ehrburger-Dolle, F.; Morfin, I.; Bley, F.; Aguilar De Armas, M. R.; López Donaire, M. L.; San Roman, J.; Bölgen, N.; Piskin, E.; Ziane, O.; et al. SAXS investigation of the effect of temperature on the multiscale structure of a macroporous poly(N-isopropylacrylamide) gel. *Macromolecules* **2010**, *43*, 2009−2017.
(64) Scherdel, C.; Scherb, T.; Reichenauer, G. Spherical porous carbon particles derived from suspensions and sediments of resorcinol-formaldehyde particles. *Carbon* **2009**, *47*, 2244−2252.

DOI: 10.1021/acs.jpcc.5b09556
J. Phys. Chem. C 2016, 120, 1488−1506

(65) Pollock, R. A.; Walsh, B. R.; Fry, J.; Ghampson, I. T.; Melnichenko, Y. B.; Kaiser, H.; Pynn, R.; Desisto, W. J.; Wheeler, M. C.; Frederick, B. G. Size and spatial distribution of micropores in SBA-15 using CM-SANS. *Chem. Mater.* **2011**, *23*, 3828−3840.
(66) McDonald, M. J.; Smith, J. W. H.; Dahn, J. R. A study of small angle x-ray scattering from impregnated activated carbons. *Carbon* **2014**, *68*, 452−461.
(67) Beaucage, G.; Schaefer, D. W. Structural studies of complex systems using small-angle scattering: a unified Guinier/power-law approach. *J. Non-Cryst. Solids* **1994**, *172*−*174*, 797−805.
(68) Goderis, B.; Reynaers, H.; Koch, M. H. J.; Mathot, V. B. F. Use of SAXS and linear correlation functions for the determination of the crystallinity and morphology of semicrystalline polymers. Application to linear polyethylene. *J. Polym. Sci., Part B: Polym. Phys.* **1999**, *37*, 1715−1738.
(69) Gouze, B.; Cambedouzou, J.; Parrès-Maynadié, S.; Rébiscoul, D. How hexagonal mesoporous silica evolves in water on short and long term: role of pore size and silica wall porosity. *Microporous Mesoporous Mater.* **2014**, *183*, 168−176.
(70) Van De Vyver, S.; Peng, L.; Geboers, J.; Schepers, H.; De Clippel, F.; Gommes, C. J.; Goderis, B.; Jacobs, P. A.; Sels, B. F. Sulfonated silica/carbon nanocomposites as novel catalysts for hydrolysis of cellulose to glucose. *Green Chem.* **2010**, *12*, 1560−1563.
(71) Albouy, P. A.; Ayral, A. Coupling x-ray scattering and nitrogen adsorption: an interesting approach for the characterization of ordered mesoporous materials. Application to hexagonal silica. *Chem. Mater.* **2002**, *14*, 3391−3397.
(72) Zickler, G. A.; Jähnert, S.; Wagermaier, W.; Funari, S. S.; Findenegg, G. H.; Paris, O. Physisorbed films in periodic mesoporous silica studied by in situ synchrotron small-angle diffraction. *Phys. Rev. B: Condens. Matter Mater. Phys.* **2006**, *73*, 184109.
(73) Muroyama, N.; Yoshimura, A.; Kubota, Y.; Miyasaka, K.; Ohsuna, T.; Ryoo, R.; Ravikovitch, P. I.; Neimark, A. V.; Takata, M.; Terasaki, O. Argon adsorption on MCM-41 mesoporous crystal studied by in situ synchrotron powder x-ray diffraction. *J. Phys. Chem. C* **2008**, *112*, 10803−10813.
(74) Zhao, D.; Huo, Q.; Feng, J.; Chmelka, B.; Stucky, G. Nonionic triblock and star diblock copolymer and oligomeric sufactant syntheses of highly ordered, hydrothermally stable, mesoporous silica structures. *J. Am. Chem. Soc.* **1998**, *120*, 6024−6036.
(75) Dunlop, J. W. C.; Fratzl, P. Multilevel architectures in natural materials. *Scr. Mater.* **2013**, *68*, 8−12.
(76) Kirkensgaard, J. J. K.; Evans, M. E.; De Campo, L. H.; Hyde, S. T. Hierarchical self-assembly of a striped gyroid formed by threaded chiral mesoscale networks. *Proc. Natl. Acad. Sci. U. S. A.* **2014**, *111*, 1271−1276.
(77) Ciccariello, S. Small-angle techniques for the asymptotic analysis of x-ray diffraction peaks. *Acta Crystallogr., Sect. A: Found. Crystallogr.* **1990**, *46*, 175−186.
(78) Solovyov, L. A.; Kirik, S. D.; Shmakov, A. N.; Romannikov, V. N. X-ray structural modeling of silicate mesoporous mesophase material. *Microporous Mesoporous Mater.* **2001**, *44*−*45*, 17−23.
(79) Mascotto, S.; Wallacher, D.; Brandt, A.; Hauss, T.; Thommes, M.; Zickler, G. A.; Funari, S. S.; Timmann, A.; Smarsly, B. M. Analysis of microporosity in ordered mesoporous hierarchically structured silica by combining physisorption with in situ small-angle scattering (SAXS and SANS). *Langmuir* **2009**, *25*, 12670−12681.
(80) Sundblom, A.; Oliveira, C. L. P.; Palmqvist, A. E. C.; Pedersen, J. S. Modeling in situ small-angle x-ray scattering measurements following the formation of mesostructured silica. *J. Phys. Chem. C* **2009**, *113*, 7706−7713.
(81) Matheron, G. *Random Sets and Integral Geometry*; Wiley: New York, 1975.
(82) Gille, W. Scattering properties and structure functions of Boolean models. *Comput. Struct.* **2011**, *89*, 2309−2315.

DOI: 10.1021/acs.jpcc.5b09556
J. Phys. Chem. C 2016, 120, 1488−1506